AMES GRANT
IN-34-CR
7625
P 27

MCAT Institute Final Report 91--002

COMPUTATION OF VISCOUS BLAST WAVE FLOWFIELDS

Christopher A. Atwood

FINAL REPORT
FOR THE PERIOD June 1, 1988 to May 31, 1990

(NASA-CR-188080) COMPUTATION OF VISCOUS BLAST WAVE FLOWFIELDS Final Report, 1 Jun. 1988 - 31 May 1990 (MCAT Inst.) 27 p
CSCL 20D
N91-22512
Unclas
G3/34 0007625

March 1991

NCC 2-540

MCAT Institute
3933 Blue Gum Drive
San Jose, California 95127

MCAT Institute Final Report 91--002

COMPUTATION OF VISCOUS BLAST WAVE FLOWFIELDS

Christopher A. Atwood

FINAL REPORT
FOR THE PERIOD June 1, 1988 to May 31, 1990

March 1991

MCAT Institute
3933 Blue Gum Drive
San Jose, California 95127

COMPUTATION OF VISCOUS BLAST WAVE FLOWFIELDS

Christopher A. Atwood

The study of the effects of blast-wave impingment upon vehicles and structures is of practical consideration in the determination of their survivability. Unfortunately, the experimental study of the blast-wave/target interaction problem is expensive, and detailed flowfield quantities are difficult to obtain. However, recent advances in computational fluid dynamics may provide a means, complementary to experimental studies, by which the timely design of effective configurations can be found.

A method to determine unsteady solutions of the Navier-Stokes equations has been developed and applied. The structured finite-volume, approximately factored implicit scheme uses Newton subiterations to obtain the spatially and temporally second-order accurate time history of the interaction of bast-waves with stationary targets. The inviscid flux is evaluated using MacCormack's modified Steger-Warming flux or Roe flux difference splittings with total variation diminishing limiters, while the viscous flux is computed using central differences. The use of implicit boundary conditions in conjunction with a telescoping in time and space method permitted solutions to this strongly unsteady class of problems. Comparisons of numerical, analytical, and experimental results have been made in two and three dimensions. These comparisons revealed accurate wave speed resolution with nonoscillatory discontinuity capturing.

The simulation of the inviscid blast-wave problem has been studied in the past by Champney, Chaussee, and Kutler; by Mark and Kutler; and by Lohner and Yee. The addition of viscous effects has been studied in two dimensions by Bennett, Abbett, and Wolf; by Molvik; and by Hisley and Molvik. The purpose of this effort was to address the three-dimensional, viscous blast-wave problem.

Test cases were undertaken to reveal these methods' weaknesses in three regimes: 1) viscous-dominated flow; 2) complex unsteady flow; and 3) three-dimensional flow. Comparisons of these computations to analytic and experimental results provided initial validation of the resultant code. Additional details on the numerical method and on the validation can be found in Appendix A. Presently, the code which has been released is capable of single zone computations with selection of any permutation of solid wall or flow-through boundaries.

The disadvantage of these characteristic-based schemes is their expense: 86 μs/cell/iteration at 140 MFLOPS on a single head of the CCF ray Y-MP/832. However, memory use is a conventional 38 words/cell. Incorporation of a zonal methodology, a turbulence model and time metrics would increase the versatility of the present code.

APPENDIX A

AIAA-90-3100-CP

An Upwind Approach to Unsteady Flowfield Simulation

Christopher A. Atwood*
MCAT Institute, NASA Ames Research Center
Moffett Field, California 94035-1000

Abstract

A numerical method to determine unsteady solutions of the laminar, perfect gas Navier-Stokes equations has been developed. The structured finite-volume, approximately factored implicit scheme uses Newton subiterations to obtain the spatially and temporally second-order accurate time history of the interaction of blast-waves with stationary targets. The inviscid flux is evaluated using either of two upwind techniques, while the viscous terms are computed by central differencing. Comparisons of numerical, analytical, and experimental results are made in two and three dimensions. The results show accurate wave speed resolution and nonoscillatory discontinuity capturing.

Nomenclature

A, B, C	inviscid flux Jacobians
c	speed of sound
c_p	specific heat at constant pressure
c_v	specific heat at constant volume
e	total energy per unit volume
E, F, G	flux vectors
$\vec{F}$	flux tensor of second order
h	enthalpy per unit mass
$\mathbf{i}, \mathbf{j}, \mathbf{k}$	Cartesian unit vectors
J	coordinate transformation Jacobian
k	coefficient of thermal conductivity
M	Mach number or viscous flux Jacobian
p	static pressure
Pr	Prandtl number
q	velocity magnitude
$\mathbf{q}$	heat transfer vector
Q	vector of dependent variables
R	specific gas constant
Re	Reynolds number
$\mathbf{r}$	position vector in physical space
s	entropy function
$\mathbf{s}$	outward-directed surface normal
t	time
T	absolute temperature
T^{-1}, T	matrices of left and right eigenvectors
u, v, w	Cartesian velocity components
U, V, W	contravariant velocities
$\mathcal{V}$	volume
x, y, z	Cartesian physical space coordinates
β	compression parameter
γ	ratio of specific heats
ϵ	internal energy per unit mass
ζ	bulk coefficient of viscosity
κ	ratio of coefficient of thermal conductivity to the specific heat at constant volume
λ	second coefficient of viscosity
Λ	diagonal matrix of eigenvalues, λ_i
μ	dynamic or first coefficient of viscosity
ξ, η, ζ	curvilinear space coordinates
ρ	density
τ	computational temporal coordinate
τ_{ij}	viscous stress tensor
ϕ	flux influence parameter

Superscripts

j	wave family
m	subiteration level
n	time level

Subscripts

i, j, k	ξ, η, ζ direction indices
NS	Navier-Stokes
T	total or stagnation quantity
x, y, z	partial with respect to Cartesian coordinate
ξ, η, ζ	partial w.r.t. curvilinear coordinate

Introduction

The study of the effects of blast-wave impingment upon vehicles and structures is of practical consideration in the determination of their survivability. The experimental study of the blast-wave/target interaction problem is expensive, and detailed flowfield quantities are difficult to obtain. Recent advances in computational fluid dynamics may provide a means, complementary to experimental studies, by which the timely design of effective configurations can be found.

The simulation of the inviscid blast-wave problem has been studied in the past by Champney, Chaussee, and Kutler,[1] Mark and Kutler,[2] Löhner,[3] and Yee.[4] The addition of viscous effects has been studied in two dimensions by Bennett, Abbett, and Wolf,[5] Molvik,[6]

---

* Research Scientist, Member AIAA.

and Hisley and Molvik.[7] The purpose of this effort is to address the three-dimensional, viscous blast-wave problem.

The techniques developed here utilize total variation diminishing (TVD) upwind and upwind-biased schemes to resolve the discontinuous flow features without the oscillations prevalent in the more conventional of the central difference methods. Wave speeds are resolved adequately at large Courant numbers through the use of time conservative differencing and Newton subiterations to retain accuracy.

The following sections provide background material on the assumptions made, the analysis of the implicit scheme, and the flux evaluation methods. The extensions of previous work are also noted. Finally, the methods are applied to five test cases, including comparisons of numerical, analytical, and experimental results.

The Governing Equations

The Navier-Stokes Equations

The Navier-Stokes equations may be expressed in integral conservation law form, coupled with the continuity and energy equations as

$$\frac{\partial}{\partial t}\left(\frac{1}{\mathcal{V}}\int_{\mathcal{V}} Q d\mathcal{V}\right) + \frac{1}{\mathcal{V}}\oint_{S} \vec{F}\cdot ds = 0 \qquad (1)$$

where body forces have been neglected and the cell volumes are time invariant. Here $\mathcal{V}$ is the volume of an arbitrary fluid packet, $\vec{F}$ is the flux tensor of second order, and ds is an outward directed normal of a differential surface area. The vectors may be written in Cartesian coordinates as

$$Q = [\rho, \rho u, \rho v, \rho w, e]^T$$

$$E_{NS} = \begin{bmatrix} \rho u \\ \rho u^2 + p + \tau_{xx} \\ \rho uv + \tau_{xy} \\ \rho uw + \tau_{xz} \\ (e+p)u + \tau_{xx}u + \tau_{xy}v + \tau_{xz}w + q_x \end{bmatrix}$$

$$F_{NS} = \begin{bmatrix} \rho v \\ \rho vu + \tau_{yx} \\ \rho v^2 + p + \tau_{yy} \\ \rho vw + \tau_{yz} \\ (e+p)v + \tau_{yx}u + \tau_{yy}v + \tau_{yz}w + q_y \end{bmatrix}$$

$$G_{NS} = \begin{bmatrix} \rho w \\ \rho wu + \tau_{zx} \\ \rho wv + \tau_{zy} \\ \rho w^2 + p + \tau_{zz} \\ (e+p)w + \tau_{zx}u + \tau_{zy}v + \tau_{zz}w + q_z \end{bmatrix}$$

where each flux can be partitioned into inviscid and viscous portions. The viscous portion is composed of the terms:

$$\begin{aligned}
\tau_{xx} &= -2\mu\frac{\partial u}{\partial x} - \lambda\left(\frac{\partial u}{\partial x} + \frac{\partial v}{\partial y} + \frac{\partial w}{\partial z}\right) \\
\tau_{yy} &= -2\mu\frac{\partial v}{\partial y} - \lambda\left(\frac{\partial u}{\partial x} + \frac{\partial v}{\partial y} + \frac{\partial w}{\partial z}\right) \\
\tau_{zz} &= -2\mu\frac{\partial w}{\partial z} - \lambda\left(\frac{\partial u}{\partial x} + \frac{\partial v}{\partial y} + \frac{\partial w}{\partial z}\right) \\
\tau_{xy} &= \tau_{yx} = -\mu\left(\frac{\partial u}{\partial y} + \frac{\partial v}{\partial x}\right) \\
\tau_{xz} &= \tau_{zx} = -\mu\left(\frac{\partial u}{\partial z} + \frac{\partial w}{\partial x}\right) \\
\tau_{yz} &= \tau_{zy} = -\mu\left(\frac{\partial v}{\partial z} + \frac{\partial w}{\partial y}\right)
\end{aligned}$$

The total energy per unit volume is related to the internal energy per unit mass by $e = \rho\epsilon + \rho q^2/2$. The perfect gas equation of state, $p = \rho RT$, completes the system. In addition, for thermally and calorically perfect gases the specific heats are constant, leaving $\epsilon = c_v T$, and $h = c_p T$. The ratio of specific heats is taken as $\gamma = \frac{c_p}{c_v} = 1.4$, and the thermodynamic states are related using

$$h_T = \frac{(e+p)}{\rho}, \quad e = \frac{p}{\gamma - 1} + \frac{\rho}{2}(u^2 + v^2 + w^2)$$

Fourier's law for heat transfer by conduction is assumed; hence, the heat transfer can be expressed as

$$\begin{aligned}
\mathbf{q} &= -k\nabla T = -(q_x\mathbf{i} + q_y\mathbf{j} + q_z\mathbf{k}) \\
&= -\kappa\left(\frac{\partial \epsilon}{\partial x}\mathbf{i} + \frac{\partial \epsilon}{\partial y}\mathbf{j} + \frac{\partial \epsilon}{\partial z}\mathbf{k}\right)
\end{aligned}$$

where $\kappa = k/c_v = \gamma\mu/Pr$. The Prandtl number for air is fixed at $Pr = 0.72$.

The relationship between the first (μ), second (λ), and bulk (ζ) viscosity coefficients is $\zeta = \frac{2}{3}\mu + \lambda$. The bulk viscosity coefficient is set to zero in accordance with Stokes' hypothesis, resulting in $\lambda = -2/3\mu$. Viscosity is related to the thermodynamic state using Sutherland's formula:

$$\mu = \frac{C_1 T^{\frac{3}{2}}}{T + C_2}$$

where C_1 and C_2 are specific to the gas in question.

A solution to this system of nonlinear partial differential equations may be obtained numerically over a discretized domain, which in turn is frequently transformed into a convenient computational space.

Transformation to Curvilinear Coordinates

In order to adequately resolve the solid boundary/fluid interaction, it is common to transform the above equations into curvilinear coordinates which can be body-conformal. Specifically, the body is constrained to lie at a constant ξ, η, or ζ value. For a stationary grid, this transformation can be expressed as

$$\tau = t,\ \xi = \xi(x,y,z),\ \eta = \eta(x,y,z),\ \zeta = \zeta(x,y,z)$$

Application of the chain rule of differentiation yields

$$\frac{\partial}{\partial x} = \xi_x \frac{\partial}{\partial \xi} + \eta_x \frac{\partial}{\partial \eta} + \zeta_x \frac{\partial}{\partial \zeta}$$

with similar expressions for the partials with respect to y and z. The inverse transformation gives

$$\frac{\partial}{\partial \xi} = x_\xi \frac{\partial}{\partial x} + y_\xi \frac{\partial}{\partial y} + z_\xi \frac{\partial}{\partial z}$$

Again, expressions can be found for the η and ζ partials in a like manner. Represented in matrix form:

$$\begin{bmatrix} \frac{\partial}{\partial x} \\ \frac{\partial}{\partial y} \\ \frac{\partial}{\partial z} \end{bmatrix} = \underbrace{\begin{bmatrix} \xi_x & \eta_x & \zeta_x \\ \xi_y & \eta_y & \zeta_y \\ \xi_z & \eta_z & \zeta_z \end{bmatrix}}_{T} \begin{bmatrix} \frac{\partial}{\partial \xi} \\ \frac{\partial}{\partial \eta} \\ \frac{\partial}{\partial \zeta} \end{bmatrix}$$

and for the inverse transformation,

$$\begin{bmatrix} \frac{\partial}{\partial \xi} \\ \frac{\partial}{\partial \eta} \\ \frac{\partial}{\partial \zeta} \end{bmatrix} = \underbrace{\begin{bmatrix} x_\xi & y_\xi & z_\xi \\ x_\eta & y_\eta & z_\eta \\ x_\zeta & y_\zeta & z_\zeta \end{bmatrix}}_{T^{-1}} \begin{bmatrix} \frac{\partial}{\partial x} \\ \frac{\partial}{\partial y} \\ \frac{\partial}{\partial z} \end{bmatrix}$$

Combining the use of $T = (T^{-1})^{-1}$ and finite volume metrics, such as those described by Vinokur,[8] leads to a scheme which is freestream-preserving because of the telescoping property. Hence, if the surface normals to a constant ξ, η, or ζ plane are defined respectively as

$$\begin{aligned}
\mathbf{s}_{i+\frac{1}{2}} &= s_{x,i+\frac{1}{2}}\mathbf{i} + s_{y,i+\frac{1}{2}}\mathbf{j} + s_{z,i+\frac{1}{2}}\mathbf{k} \\
&= \frac{1}{2}(\mathbf{r}_7 - \mathbf{r}_4) \times (\mathbf{r}_8 - \mathbf{r}_3) \\
\mathbf{s}_{j+\frac{1}{2}} &= s_{x,j+\frac{1}{2}}\mathbf{i} + s_{y,j+\frac{1}{2}}\mathbf{j} + s_{z,j+\frac{1}{2}}\mathbf{k} \\
&= \frac{1}{2}(\mathbf{r}_7 - \mathbf{r}_2) \times (\mathbf{r}_3 - \mathbf{r}_6) \\
\mathbf{s}_{k+\frac{1}{2}} &= s_{x,k+\frac{1}{2}}\mathbf{i} + s_{y,k+\frac{1}{2}}\mathbf{j} + s_{z,k+\frac{1}{2}}\mathbf{k} \\
&= \frac{1}{2}(\mathbf{r}_6 - \mathbf{r}_8) \times (\mathbf{r}_5 - \mathbf{r}_7)
\end{aligned}$$

where the index convention is shown in Fig. 1, then the metrics can be formed as

$$\begin{aligned}
\xi_x &= J(y_\eta z_\zeta - y_\zeta z_\eta) = \frac{1}{\mathcal{V}} s_{x,i+\frac{1}{2}} \\
\xi_y &= J(x_\zeta z_\eta - x_\eta z_\zeta) = \frac{1}{\mathcal{V}} s_{y,i+\frac{1}{2}} \\
\xi_z &= J(x_\eta y_\zeta - x_\zeta y_\eta) = \frac{1}{\mathcal{V}} s_{z,i+\frac{1}{2}} \\
\eta_x &= J(y_\zeta z_\xi - y_\xi z_\zeta) = \frac{1}{\mathcal{V}} s_{x,j+\frac{1}{2}} \\
\eta_y &= J(x_\xi z_\zeta - x_\zeta z_\xi) = \frac{1}{\mathcal{V}} s_{y,j+\frac{1}{2}} \\
\eta_z &= J(x_\zeta y_\xi - x_\xi y_\zeta) = \frac{1}{\mathcal{V}} s_{z,j+\frac{1}{2}} \\
\zeta_x &= J(y_\xi z_\eta - y_\eta z_\xi) = \frac{1}{\mathcal{V}} s_{x,k+\frac{1}{2}} \\
\zeta_y &= J(x_\eta z_\xi - x_\xi z_\eta) = \frac{1}{\mathcal{V}} s_{y,k+\frac{1}{2}} \\
\zeta_z &= J(x_\xi y_\eta - x_\eta y_\xi) = \frac{1}{\mathcal{V}} s_{z,k+\frac{1}{2}}
\end{aligned}$$

These metrics represent the projections of the cell face normal into (x, y, z) space. The faces of the hexahedron exactly enclose the discrete control volume, i.e., no gaps are permitted at the edges. Finally, the Jacobian of the coordinate transformation is equivalent to the inverse of the volume, as related by

$$\begin{aligned}
\frac{1}{J} &= \frac{\partial(x,y,z)}{\partial(\xi,\eta,\zeta)} \\
&= x_\xi(y_\eta z_\zeta - y_\zeta z_\eta) - x_\eta(y_\xi z_\zeta - y_\zeta z_\xi) \\
&\quad + x_\zeta(y_\xi z_\eta - y_\eta z_\xi) \\
&= \mathcal{V} = \frac{1}{3}(\mathbf{s}_{i-\frac{1}{2}} + \mathbf{s}_{j-\frac{1}{2}} + \mathbf{s}_{k-\frac{1}{2}}) \cdot (\mathbf{r}_7 - \mathbf{r}_1)
\end{aligned}$$

Utilizing these metrics in the application of the chain rule to Eq. (1) and subsequent simplification yields

$$Q'_\tau + E'_\xi + F'_\eta + G'_\zeta = 0$$

where

$$\begin{aligned}
Q' &= Q\mathcal{V} \\
E'_{NS} &= (E_{NS}\xi_x + F_{NS}\xi_y + G_{NS}\xi_z)\mathcal{V} \\
&= [E_{NS}s_x + F_{NS}s_y + G_{NS}s_z|_i \\
F'_{NS} &= (E_{NS}\eta_x + F_{NS}\eta_y + G_{NS}\eta_z)\mathcal{V} \\
&= [E_{NS}s_x + F_{NS}s_y + G_{NS}s_z|_j \\
G'_{NS} &= (E_{NS}\zeta_x + F_{NS}\zeta_y + G_{NS}\zeta_z)\mathcal{V} \\
&= [E_{NS}s_x + F_{NS}s_y + G_{NS}s_z|_k
\end{aligned}$$

Separating the inviscid and viscous portions of the flux vectors, in the ξ direction $E'_{NS} = E' + E'_v$, then

$$E' = \mathcal{V} \begin{bmatrix} \rho U \\ \rho u U + \xi_x p \\ \rho v U + \xi_y p \\ \rho w U + \xi_z p \\ (e+p)U \end{bmatrix}$$

Here the contravariant velocity is $U = u\xi_x + v\xi_y + w\xi_z$, without metric normalization. The viscous flux can be represented as

$$E'_v = \mathcal{V} \begin{bmatrix} 0 \\ \tau_{xx}\xi_x + \tau_{yx}\xi_y + \tau_{zx}\xi_z \\ \tau_{xy}\xi_x + \tau_{yy}\xi_y + \tau_{zy}\xi_z \\ \tau_{xz}\xi_x + \tau_{yz}\xi_y + \tau_{zz}\xi_z \\ (ue'_2 + ve'_3 + we'_4) + (q_x\xi_x + q_y\xi_y + q_z\xi_z) \end{bmatrix}$$

where the viscous stress terms are evaluated by again invoking the chain rule, and the flux in the η and ζ directions are found similarly. The results presented herein are implemented using either the thin-layer or the full viscous term treatment.

The widespread use of the thin-layer approximation, first implemented by Steger,[9] can be justified from either physical or algorithmical arguments. Physically, the neglect of all diffusion processes parallel to the body is similar to that used in boundary-layer theory, albeit not as restrictive. Hence, when the viscous effects are confined to thin regions which fall along a constant ξ, η, or ζ plane then this assumption is valid. Algorithmically, the banded matrix structure used in multidimensional algorithms which sequentially solve a set of unidirectional problems can include only these thin-layer terms implicitly. This thin-layer flux in the η direction, assumed to be the body normal coordinate, is expressed as:

$$F'_{tl} = -\mathcal{V} \begin{bmatrix} 0 \\ m_1 u_\eta + m_4 v_\eta + m_5 w_\eta \\ m_4 u_\eta + m_2 v_\eta + m_6 w_\eta \\ m_5 u_\eta + m_6 v_\eta + m_3 w_\eta \\ m_1 \bar{u} u_\eta + m_2 \bar{v} v_\eta + m_3 \bar{w} w_\eta \\ + m_4(\bar{u} v_\eta + \bar{v} u_\eta) + m_5(\bar{u} w_\eta + \bar{w} u_\eta) \\ + m_6(\bar{v} w_\eta + \bar{w} v_\eta) + \kappa \epsilon_\eta (\eta_x^2 + \eta_y^2 + \eta_z^2) \end{bmatrix}$$

where the ($\bar{\ }$) denotes an arithmetic mean value and

$$\begin{aligned} m_1 &= \mu\left(\frac{4}{3}\eta_x^2 + \eta_y^2 + \eta_z^2\right), & m_4 &= \frac{\mu}{3}\eta_x\eta_y \\ m_2 &= \mu\left(\eta_x^2 + \frac{4}{3}\eta_y^2 + \eta_z^2\right), & m_5 &= \frac{\mu}{3}\eta_x\eta_z \\ m_3 &= \mu\left(\eta_x^2 + \eta_y^2 + \frac{4}{3}\eta_z^2\right), & m_6 &= \frac{\mu}{3}\eta_y\eta_z \end{aligned}$$

These viscous flux terms may be found for the remaining spatial coordinates as well. The results presented here are implemented using either the thin-layer or the full viscous term treatment, as required by the the flow physics.

Nondimensionalization

The governing equations may be nondimensionalized by the choice of a length scale, denoted $\tilde{L}$, and reference values of ρ, u, and p such as

$$\tilde{\rho}_{ref} = \tilde{\rho}_\infty, \quad \tilde{u}_{ref} = \sqrt{\tilde{p}_\infty / \tilde{\rho}_\infty}, \quad \tilde{p}_{ref} = \tilde{p}_\infty$$

The remaining variables follow:

$$\begin{aligned} &\rho = \tilde{\rho}/\tilde{\rho}_{ref}, && p = \tilde{p}/\tilde{p}_{ref}, && e = \tilde{e}/(\tilde{\rho}_{ref}\tilde{u}^2_{ref}) \\ &u = \tilde{u}/\tilde{u}_{ref}, && v = \tilde{v}/\tilde{u}_{ref}, && w = \tilde{w}/\tilde{u}_{ref} \\ &t = \tilde{t}\tilde{u}_{ref}/\tilde{L}, && T = p/\rho, && \mu = \tilde{\mu}_{,}/\tilde{\mu}_{ref} \end{aligned}$$

The Reynolds number resulting from this procedure is $Re = \tilde{\rho}_{ref}\tilde{L}\tilde{u}_{ref}/\tilde{\mu}_{ref}$, where the ($\tilde{\ }$) denotes a dimensional quantity, and the ($_\infty$) denotes the quiescent conditions surrounding the target before primary shock arrival.

The Numerical Technique

The development of the scheme will be described by discussion of the first-order terms, following which the higher-order extensions will be outlined. The scheme as expressed for a cell which has a mean flux value on each of the six sides is

$$\begin{aligned} &\frac{\partial}{\partial\tau}\int_{\mathcal{V}} Q\,d\mathcal{V} \\ &\quad + \int_{j-\frac{1}{2}}^{j+\frac{1}{2}}\int_{k-\frac{1}{2}}^{k+\frac{1}{2}} (E'_{i+\frac{1}{2},j,k} - E'_{i-\frac{1}{2},j,k})\,d\zeta\,d\eta \\ &\quad + \int_{k-\frac{1}{2}}^{k+\frac{1}{2}}\int_{i-\frac{1}{2}}^{i+\frac{1}{2}} (F'_{i,j+\frac{1}{2},k} - F'_{i,j-\frac{1}{2},k})\,d\xi\,d\zeta \\ &\quad + \int_{i-\frac{1}{2}}^{i+\frac{1}{2}}\int_{j-\frac{1}{2}}^{j+\frac{1}{2}} (G'_{i,j,k+\frac{1}{2}} - G'_{i,j,k-\frac{1}{2}})\,d\eta\,d\xi = 0 \end{aligned}$$

In discrete form, after dropping the primes for convenience, the governing equations can be written as

$$\begin{aligned} Q^{n+1}_{i,j,k} - Q^n_{i,j,k} \quad &+ \quad \frac{\Delta\tau}{\mathcal{V}_{i,j,k}}\Big\{(E^{n+1}_{i+\frac{1}{2},j,k} - E^{n+1}_{i-\frac{1}{2},j,k}) \\ &+ \quad (F^{n+1}_{i,j+\frac{1}{2},k} - F^{n+1}_{i,j-\frac{1}{2},k}) \\ &+ \quad (G^{n+1}_{i,j,k+\frac{1}{2}} - G^{n+1}_{i,j,k-\frac{1}{2}})\Big\} = 0 \end{aligned}$$

where n denotes the time level in this implicit representation, and $\Delta\xi$, $\Delta\eta$, and $\Delta\zeta$ are set to unity for convenience.

These flux terms may be evaluated using a technique which may be broadly classed as either central or upwind. The latter technique is chosen for this study for the desirable numerical properties, such as diagonal dominance of the flux Jacobian, and for the physical dependence on zones of influence which are inherent in upwind schemes.

Upwind Schemes

Upwind schemes bias the derivative evaluations required to determine the flux across fluid cells according to the sign of the eigenvalues. In this manner these methods bring the physics of the hyperbolic system, the unsteady Euler equations, into the numerical solution process. To facilitate the implementation of these upwind schemes, the eigensystem is determined. The similarity transformation which diagonalizes the unsteady, inviscid, gas-dynamic equations, shown by Warming, Beam, and Hyett,[10] is outlined as follows

$$E = AQ = T\Lambda T^{-1}Q$$

where the rows of T^{-1} are the eigenvectors and

$$\Lambda = \Lambda^+ + \Lambda^- = \; diag\left[\hat{U}, \hat{U}, \hat{U}, \hat{U} + c, \hat{U} - c\right] \|s\|$$

using normalized contravariant velocities. The eigenvalues can be split according to, among other splittings, their signs:

$$\lambda^\pm \;=\; \frac{\lambda \pm |\lambda|}{2}$$

Two upwind schemes are implemented here to compare the results which may be obtained with either of the techniques. The early portion of this discussion will be shown unidimensionally; the multidimensional extension will be outlined towards the end of this section.

Flux Vector Splitting

The shock-capturing scheme developed by Steger and Warming[11] revisited the classical characteristic procedures. They found that the Euler equations possessed the property of homogeneity of degree one for the equation of state used here, meaning $E(\alpha Q) = \alpha E(Q)$. For a vector with this property $E = AQ$ and consequently the flux vector can be split into two parts, each physically corresponding to the right and left moving waves. This technique resulted in the flux being represented as a combination of the subspaces associated with the positive and negative eigenvalues, expressed as

$$\begin{aligned} E &= T(\Lambda^+ + \Lambda^-)T^{-1}Q \;=\; (A^+ + A^-)Q \\ &= E^+ + E^- \end{aligned}$$

where T and T^{-1} are the right and left eigenvectors, respectively. The flux across a cell face can be determined by

$$\begin{aligned} E_{i+\frac{1}{2}} &= E^+_{i+\frac{1}{2}} + E^-_{i+\frac{1}{2}} \\ &= A^+_{i+\frac{1}{2}}Q_{i,j} + A^-_{i+\frac{1}{2}}Q_{i+1} \end{aligned}$$

Because the Jacobian at $i + \frac{1}{2}$ is dependent on two states, this solution method now diverges from the original flux vector splitting. The treatment of this Jacobian is shown in a following section. Linearization in time can be performed for one flux as follows, the extension to the remaining flux terms is omitted for brevity. At the $n + 1$ time level,

$$\begin{aligned} E^{n+1}_{i+\frac{1}{2}} &= (A^+)^{n+1}_{i+\frac{1}{2}}Q^{n+1}_i + (A^-)^{n+1}_{i+\frac{1}{2}}Q^{n+1}_{i+1} \\ &= (A^+)^n_{i+\frac{1}{2}}\delta Q_i + (A^-)^n_{i+\frac{1}{2}}\delta Q_{i+1} + E^n_{i+\frac{1}{2}} \end{aligned}$$

where the implicit change in the dependent variables is given by $\delta Q = Q^{n+1} - Q^n$. Note that the Jacobian matrices are frozen at time level n. The remaining flux, $E^{n+1}_{i-\frac{1}{2}}$, may be obtained similarly.

To assess the effect on stability of this type of linearization, a procedure given by Barth[12] is applied to this method. Using the semidiscrete form $\partial Q_i/\partial t = -R_i$, then

$$R_i = \frac{1}{\Delta x}\left(E_{i+\frac{1}{2}} - E_{i-\frac{1}{2}}\right)$$

Using frozen Jacobian matrices, the method can be linearized as follows:

$$\left[\frac{I}{\Delta t} + \left(\frac{\partial R}{\partial Q}\right)^n\right]\delta Q = -R^n \qquad (2)$$

where for the first-order subset the Jacobian is a block tridiagonal matrix. The blocks along the i^{th} row are

$$\begin{aligned} \frac{\partial R_i}{\partial Q_{i-1}} &= \frac{1}{\Delta x}\left(-A^+_{i-\frac{1}{2}}\right) \\ \frac{\partial R_i}{\partial Q_i} &= \frac{1}{\Delta x}\left(A^+_{i+\frac{1}{2}} - A^-_{i-\frac{1}{2}}\right) \\ \frac{\partial R_i}{\partial Q_{i+1}} &= \frac{1}{\Delta x}\left(A^-_{i+\frac{1}{2}}\right) \end{aligned}$$

This scheme is inherently conservative in space because of the telescoping property of the finite-volume formulation; analysis of this scheme reveals that it is also conservative in time, thus allowing the use of large Courant numbers. A demonstration of this analysis proceeds by writing the scheme as

$$\left[\frac{I}{\Delta t} + A^n\right]\delta Q = -R^n = -A^nQ^n$$

hence

$$Q^{n+1} + \Delta t A^n Q^{n+1} = Q^n \qquad (3)$$

In order for the scheme to be conservative in time over a periodic domain, the global average of a solution must remain constant for all time, i.e., $\sum_{i=1}^{I} Q^0_i = \sum_{i=1}^{I} Q^n_i = \sum_{i=1}^{I} Q^{n+1}_i$. Hence, when Eq. (3) is summed across the domain, the result is that the columns of A^n must sum to zero. For the scheme outlined here, this can be verified with some effort. Use of these linearizations obviates the need for convergence at the subiteration level to obtain time conservation.

Flux Difference Splitting

Flux difference splitting methods are based on the Riemann problem, solved exactly by Godunov in 1959.[13] The Riemann problem is composed of $m + 1$ piecewise constant states separated by m wave families. The waves include shocks, contact surfaces, and rarefaction fans. For each of the Riemann problem cells, the transition of the dependent variables is a function of a parameter family. The solution can be found once these transition states are known. Approximate Riemann solvers simplify the numerics of the problem by eliminating the iterative process required to find the intermediate states. Figure 2 shows a schematic of the Riemann problem with the piecewise constant states separated by the appropriate wave families. The flux through the cell face is

$$\begin{aligned} E_{i+\frac{1}{2}} &= \frac{1}{2\Delta x}\left[E_i + E_{i+1} - (\Delta E^+_{i+\frac{1}{2}} - \Delta E^-_{i+\frac{1}{2}})\right] \\ &= \frac{1}{2\Delta x}(E_i + E_{i+1} - \Delta|E|_{i+\frac{1}{2}}) \end{aligned}$$

where $|E| = |A|Q = (A^+ - A^-)Q = [T(\Lambda^+ - \Lambda^-)T^{-1}]Q$. The flux differences associated with the $+$ and $-$ traveling waves are

$$\begin{aligned} \Delta E^+_{i+\frac{1}{2}} &= (T\Lambda^+T^{-1})_{i+\frac{1}{2}}(Q_{i+1} - Q_i) \\ \Delta E^-_{i+\frac{1}{2}} &= (T\Lambda^-T^{-1})_{i+\frac{1}{2}}(Q_{i+1} - Q_i) \end{aligned}$$

Again utilizing the semidiscrete form $\partial Q_i/\partial t = -R_i$, then

$$R_i = \frac{1}{2\Delta x}\left[(E_{i+1} - E_{i-1}) - (\Delta|E|_{i+\frac{1}{2}} + \Delta|E|_{i-\frac{1}{2}})\right]$$

This method can be linearized using a procedure similar to that described previously in Eq. (2). The blocks of the i^{th} row are now expressed as

$$\begin{aligned} \frac{\partial R_i}{\partial Q_{i-1}} &= \frac{1}{2\Delta x}\left(-A_{i-1} + \frac{\partial\Delta|E|_{i-\frac{1}{2}}}{\partial Q_{i-1}}\right) \\ \frac{\partial R_i}{\partial Q_i} &= \frac{1}{2\Delta x}\left(-\frac{\partial\Delta|E|_{i+\frac{1}{2}}}{\partial Q_i} + \frac{\partial\Delta|E|_{i-\frac{1}{2}}}{\partial Q_i}\right) \\ \frac{\partial R_i}{\partial Q_{i+1}} &= \frac{1}{2\Delta x}\left(A_{i+1} - \frac{\partial\Delta|E|_{i+\frac{1}{2}}}{\partial Q_{i+1}}\right) \end{aligned}$$

Substitution of the flux difference splitting expression yields

$$\begin{aligned} \frac{\partial\Delta|E|_{i+\frac{1}{2}}}{\partial Q_{i+1}} &= \frac{\partial}{\partial Q_{i+1}}\left[|A|_{i+\frac{1}{2}}(Q_{i+1} - Q_i)\right] \\ &= |A|_{i+\frac{1}{2}} + \frac{\partial\Delta|A|_{i+\frac{1}{2}}}{\partial Q_{i+1}}(Q_{i+1} - Q_i) \end{aligned}$$

These true Jacobians are expensive to compute, and the simplification to approximate Jacobians is made as

$$\frac{\partial\Delta|E|_{i+\frac{1}{2}}}{\partial Q_{i+1}} \approx |A|_{i+\frac{1}{2}}$$

Utilizing these approximate Jacobians, the linearization proceeds as

$$\begin{aligned} E^{n+1}_{i+\frac{1}{2}} &= \frac{1}{2\Delta x}(E^{n+1}_i + E^{n+1}_{i+1} - \Delta|E|^{n+1}_{i+\frac{1}{2}}) \\ &= \frac{1}{2\Delta x}\Big[(A^n_i + |A|^n_{i+\frac{1}{2}})\delta Q_i \\ &\quad +(A^n_{i+1} - |A|^n_{i+\frac{1}{2}})\delta Q_{i+1}\Big] + E^n_{i+\frac{1}{2}} \end{aligned}$$

where $E^{n+1} = E^n + A^n\delta Q$ and $Q^{n+1} = Q^n + (\partial Q/\partial t)^n\Delta t$. The flux through the remaining faces are determined similarly. This scheme can also be shown to obey the criterion for conservation in time.

Roe Averaging

In order to determine the Jacobian at the cell face $i + \frac{1}{2}$, some function, $A = A(Q_L, Q_R)$, must be assumed, where the subscripts indicate left and right states. The location where this flux evaluation occurs is among the discrepancies between finite-difference and finite-volume schemes. The Jacobian form used here is attributable to Roe,[14] which provides an approximate solution to the Riemann problem. This Jacobian is created through the use of a parameter vector composed of a geometric-like mean of the states. The more obvious arithmetic Jacobian forms, such as $A = \frac{1}{2}(A_L + A_R)$ or $A = A(\frac{1}{2}(Q_L + Q_R))$, are not conservative forms. Conservative Jacobian forms satisfy $A(Q_L, Q_R)(Q_L - Q_R) = E_L - E_R$. Stated explicitly, the Roe averaging operation is

$$\begin{aligned} \bar\rho &= \sqrt{\rho_L\rho_R} \\ \bar u_i &= \frac{u_{iL}\sqrt{\rho_L} + u_{iR}\sqrt{\rho_R}}{\sqrt{\rho_L} + \sqrt{\rho_R}} \\ &= \frac{\rho_L u_{iL} + \bar\rho(u_{iL} + u_{iR}) + \rho_R u_{iR}}{\rho_L + 2\bar\rho + \rho_R} \\ \bar h_T &= \frac{\rho_L(h_T)_L + \bar\rho((h_T)_L + (h_T)_R) + \rho_R(h_T)_R}{\rho_L + 2\bar\rho + \rho_R} \end{aligned}$$

where a ($\bar{}$) denotes a Roe averaged quantity and the latter forms are presented as inexpensive alternative expressions. Substitution of (i) for L and ($i + 1$) for R allows the evaluation of the Jacobian at the intermediary cell face. For the flux vector splitting case described earlier, MacCormack[15] has found this average helps to alleviate excessive numerical dissipation in regions dominated by viscous effects. Roe averaged values are utilized throughout the development presented here.

Higher-Order Extensions

Spatially first-order methods frequently provide inadequate resolution of the flowfield. However, the methods discussed above can be extended to higher-order spatial accuracy by modification of the right hand side. In order to assist in the preservation of well-behaved solutions near the discontinuities admitted by the strong conservation law form of the Euler equations, a total variation diminishing technique is implemented. If the total variation of a solution is defined as $TV(u) = \sum_{i=-\infty}^{\infty}|u_{i+1} - u_i|$, then a solution which follows $TV(u^{n+1}) \leq TV(u^n)$ is TVD. The TVD constraint can be shown to result in diagonal dominance, allowing the use of relaxation schemes. In this manner the scheme may be extended to higher space accuracy thoughout the smoothly varying regions of the field, reducing the accuracy in localities of high-gradient and extrema in order to obtain sharp and oscillation-free resolution. These methods are rigorously applicable only to scalar nonlinear equations or a system of linear equations in one spatial dimension. Application of these schemes to multidimensional systems of nonlinear equations are generally not TVD. Moreover, it is not clear that the higher-order accuracy of the unidimensional problem is retained in multidimensional cases. However, the results which can be obtained demonstrate the usefulness of the technique.

Of the several methods which fall into the TVD domain,[4] the technique implemented here is one attributable to Chakravarthy and Osher,[16] the development of which follows for completeness. In this formulation, the higher-order flux can be expressed as a sum of a first-order flux, denoted $E_{i+\frac{1}{2}}$, and a flux correction term. The flux correction terms are determined by first computing the flux differences across the m wave families mentioned previously. Subsequent limiting of these flux differences and summation across the wave families results in the higher-order flux. This flux is expressed as

$$
\begin{aligned}
\widehat{E}_{j+\frac{1}{2}} = E_{i+\frac{1}{2}} \\
&-\frac{(1-\phi)}{4}\left[\sum_{i}^{m}\widetilde{dE}^{j-}_{i+\frac{1}{2}}\right]-\frac{(1+\phi)}{4}\left[\sum_{i}^{m}\widetilde{\widetilde{dE}}^{j-}_{i+\frac{1}{2}}\right] \\
&+\frac{(1+\phi)}{4}\left[\sum_{i}^{m}\widetilde{dE}^{j+}_{i+\frac{1}{2}}\right]+\frac{(1-\phi)}{4}\left[\sum_{i}^{m}\widetilde{\widetilde{dE}}^{j+}_{i-\frac{1}{2}}\right]
\end{aligned}
$$

where $(\tilde{\ })$ and $(\tilde{\tilde{\ }})$ indicate a quantity that has been limited, j is the index denoting the wave family, and i is the index assigned to a cell center. Using the notation of l^j for the rows of the left eigenvector matrix, T^{-1}, and r^j for the columns of the right eigenvector matrix, T, then the measure of the change in the dependent variables is

$$\alpha^j_{i+\frac{1}{2}} = l^j_{i+\frac{1}{2}}\cdot(Q_{i+1}-Q_i)$$

The measure of the change in the flux is defined as

$$\sigma^j = \lambda^j\alpha^j = (\lambda^{j+}+\lambda^{j-})\alpha^j$$

the eigenvalues being split as shown previously. The limited counterparts of these values are obtained as:

$$
\begin{aligned}
\tilde{\sigma}^{-}_{i+\frac{1}{2}} &= \operatorname{minmod}\left[\sigma^{-}_{i+\frac{3}{2}},\beta\sigma^{-}_{i+\frac{1}{2}}\right] \\
\tilde{\tilde{\sigma}}^{-}_{i+\frac{1}{2}} &= \operatorname{minmod}\left[\sigma^{-}_{i+\frac{1}{2}},\beta\sigma^{-}_{i+\frac{3}{2}}\right] \\
\tilde{\sigma}^{+}_{i+\frac{1}{2}} &= \operatorname{minmod}\left[\sigma^{+}_{i+\frac{1}{2}},\beta\sigma^{+}_{i-\frac{1}{2}}\right] \\
\tilde{\tilde{\sigma}}^{+}_{i-\frac{1}{2}} &= \operatorname{minmod}\left[\sigma^{+}_{i-\frac{1}{2}},\beta\sigma^{+}_{i+\frac{1}{2}}\right]
\end{aligned}
$$

This limiter returns the argument of smaller magnitude when the signs are equal, and returns zero when the arguments are of opposite sign. This procedure effectively adds dissipation locally in regions of high flux gradient and at inflection points. In this manner, monotonicity is preserved by preventing the creation of new extrema while preserving the global accuracy of the solution. While formal accuracy estimates are difficult to ascertain because of the nonlinear application of limiting to different wave families, numerical experiments have demonstrated that the global accuracy of the underlying scheme is preserved.[17]

The compression parameter, β, is restricted according to $1<\beta\leq\frac{3-\phi}{1-\phi}$ and the limiting operator is given as

$$\operatorname{minmod}(x,y) = \operatorname{sign}(x)\left(\max\{0,\min[|x|,y\operatorname{sign}(x)]\}\right)$$

The compression parameter reduces the amount of dissipation added, the range being bounded by accuracy and TVD constraints. Finally, the limited flux difference values are expressed as

$$
\begin{aligned}
\widetilde{dE}^{j-}_{i+\frac{1}{2}} &= \tilde{\sigma}^{j-}_{i+\frac{1}{2}}r_{i+\frac{1}{2}} \\
\widetilde{\widetilde{dE}}^{j-}_{i+\frac{1}{2}} &= \tilde{\tilde{\sigma}}^{j-}_{i+\frac{1}{2}}r_{i+\frac{1}{2}} \\
\widetilde{dE}^{j+}_{i+\frac{1}{2}} &= \tilde{\sigma}^{j+}_{i+\frac{1}{2}}r_{i+\frac{1}{2}} \\
\widetilde{\widetilde{dE}}^{j+}_{i-\frac{1}{2}} &= \tilde{\tilde{\sigma}}^{j+}_{i-\frac{1}{2}}r_{i-\frac{1}{2}}
\end{aligned}
$$

This asymmetric limiter is designed to modify the fluxes only in the rapidly varying portions of the flow, where nonphysical oscillations are likely to occur. Since these high-gradient regions are confined to thin regions, the dominant solution domain is differenced in accordance with the underlying scheme. Variances in the value of the compression parameter allow the fluxes to be limited for different gradient levels. This implies that use of β_{max} will cause the limiting action to be taken only in the high-gradient regions, and lower values of β will result in limiting for commensurately lower flux gradients. The variety of schemes which can be obtained using this technique are shown in Table 1.

Table 1: Summary of schemes.

ϕ	Unlimited Scheme	β_{max}	2^{nd} order TE
-1	Fully upwind	2	$\frac{1}{3}(\Delta x)^2 f_{xxx}$
$-\frac{1}{3}$	Nameless	$\frac{5}{2}$	$\frac{1}{6}(\Delta x)^2 f_{xxx}$
0	Fromm's	3	$\frac{1}{12}(\Delta x)^2 f_{xxx}$
$\frac{1}{3}$	3^{rd} Order	4	0
$\frac{1}{2}$	Low TE 2^{nd} Order	5	$-\frac{1}{24}(\Delta x)^2 f_{xxx}$
1	Central	∞	$-\frac{1}{6}(\Delta x)^2 f_{xxx}$

Here $TE = (\frac{1}{3}-\phi)(\Delta x)^2 f_{xxx}/4$ defines the leading

Uu

term of the truncation error for the unlimited form of the schemes. Local metrics have been used in the above method to maintain reasonable computational efficiency, a satisfactory approximation for grids which do not contain rapid variations.

Viscous Terms

The viscous terms are treated through central differencing about the cell faces. The explicit terms are conventionally differenced after chain-rule expansion, inclusive of the cross terms if these diffusion processes are deemed significant. The left hand side does not include these cross terms, and the resultant viscous Jacobian, employing $V = [\rho, u, v, w, \epsilon]^T$ as the primitive variable vector, is

$$M = -\begin{bmatrix} 0 & 0 & 0 & 0 & 0 \\ 0 & m_{22} & \mu s_x s_y/3 & \mu s_x s_z/3 & 0 \\ 0 & m_{23} & m_{33} & \mu s_y s_z/3 & 0 \\ 0 & m_{24} & m_{34} & m_{44} & 0 \\ 0 & m_{52} & m_{53} & m_{54} & m_{55} \end{bmatrix}$$

$$m_{22} = \mu(\frac{4}{3}s_x^2 + s_y^2 + s_z^2)\ ,\ m_{33} = \mu(s_x^2 + \frac{4}{3}s_y^2 + s_z^2)$$

$$m_{44} = \mu(s_x^2 + s_y^2 + \frac{4}{3}s_z^2)\ ,\ m_{55} = \kappa(s_x^2 + s_y^2 + s_z^2)$$

$$\begin{aligned} m_{52} &= um_{22} + vm_{23} + wm_{24} \\ m_{53} &= um_{32} + vm_{33} + wm_{34} \\ m_{54} &= um_{42} + vm_{43} + wm_{44} \end{aligned}$$

Now, expansion of the block structure gives

$$\begin{aligned}
- & \left\{\frac{\Delta t}{\mathcal{V}} A^+_{i-\frac{1}{2},j,k}\right\}\delta Q_{i-1,j,k} \\
- & \left\{\frac{\Delta t}{\mathcal{V}}\left[B^+_{i,j-\frac{1}{2},k} - \frac{1}{\mathcal{V}} M_{i,j-\frac{1}{2},k} N_{i,j-1,k}\right]\right\}\delta Q_{i,j-1,k} \\
- & \left\{\frac{\Delta t}{\mathcal{V}} C^+_{i,j,k-\frac{1}{2}}\right\}\delta Q_{i,j,k-1} \\
+ & \left\{I + \frac{\Delta t}{\mathcal{V}}\left[A^+_{i+\frac{1}{2},j,k} - A^-_{i-\frac{1}{2},j,k}\right.\right. \\
& \qquad + B^+_{i,j+\frac{1}{2},k} - B^-_{i,j-\frac{1}{2},k} \\
& \qquad + C^+_{i,j,k+\frac{1}{2}} - C^-_{i,j,k-\frac{1}{2}} \\
& \left.\left.\quad + \frac{1}{\mathcal{V}}(M_{i,j+\frac{1}{2},k} + M_{i,j-\frac{1}{2},k})N_{i,j,k}\right]\right\}\delta Q_{i,j,k} \\
+ & \left\{\frac{\Delta t}{\mathcal{V}} C^-_{i,j,k+\frac{1}{2}}\right\}\delta Q_{i,j,k+1} \\
+ & \left\{\frac{\Delta t}{\mathcal{V}}\left[B^-_{i,j+\frac{1}{2},k} - \frac{1}{\mathcal{V}} M_{i,j+\frac{1}{2},k} N_{i,j+1,k}\right]\right\}\delta Q_{i,j+1,k} \\
+ & \left\{\frac{\Delta t}{\mathcal{V}} A^-_{i+\frac{1}{2},j,k}\right\}\delta Q_{i+1,j,k} = \Delta Q_{i,j,k}
\end{aligned}$$

where $N = \partial V/\partial Q$ and only the thin-layer terms in η are shown here.

Factorization

The extension of the unidimensional techniques given above is accomplished through dimensional splitting. The method used here is that of Yanenko,[18] where the factors are chosen in the ξ, η, and ζ directions. Expressing the three-dimensional equations in compact notation as

$$(I + \frac{\Delta\tau}{\Delta\xi}A + \frac{\Delta\tau}{\Delta\eta}B + \frac{\Delta\tau}{\Delta\zeta}C)\delta Q = \Delta Q$$

then the factorization procedure yields

$$(I + \frac{\Delta\tau}{\Delta\xi}A)(I + \frac{\Delta\tau}{\Delta\eta}B)(I + \frac{\Delta\tau}{\Delta\zeta}C)\delta Q = \Delta Q$$

This system can be solved sequentially through the use of intermediary steps without loss of time accuracy. Although alternating direction implicit schemes of this type offer advantages of vectorization, the system is solved as a sequence of unidimensional problems, hence limiting the size of the time step due to stability restrictions.[19] The use of this technique here is justified by the requirement of adequate time history flow resolution, thus imposing an additional constraint on the maximum feasible time step. Application of a line Gauss-Seidel method to the second test case confirmed this hypothesis. This relaxation method offered a slightly increased stability range, but not enough to warrant its additional expense. Additionally, since for the factored scheme the flux exchange occurs at the same time level, the technique is conservative, even when convergence at the subiteration level is not attained for each time step.

Newton Iterative Technique

Reduction of the linearization and factorization errors is achieved by a Newton iterative method of the type described by Rai and Chakravarthy[20] and Rogers and Kwak[21] is utilized, albeit with the addition of allowance for a varying step size.[6] Assuming that the initial guess lies within the radius of convergence, the right hand side is converged to an arbitrary accuracy while holding time fixed. Since the right hand side includes the higher-order difference representations of the Navier-Stokes equations, these errors are eliminated at convergence. The method is discussed below where m is the iteration index and n is the conventional index denoting time level. Discretizing $Q_t + E_x = 0$ gives

$$\begin{aligned} &\frac{1}{\Delta\tau}(Q^{n+1,m+1} - Q^{n+1,m}) \\ &= \quad Q_t^{n+1,m+1} + \frac{1}{\Delta\tau}(Q^{n+1,m} - Q^n) \end{aligned}$$

$$= \frac{1}{\Delta\tau}\left[Q^{n+1,m+1} - Q^{n,m+1} - (Q^{n+1,m} - Q^n)\right]$$

Defining $\delta Q' = Q^{n+1,m+1} - Q^{n+1,m}$, then

$$\begin{aligned} I\delta Q' &= \Delta\tau Q_t^{n+1,m+1} - (Q^{n+1,m} - Q^n) \\ &= -\Delta\tau E_x^{n+1,m+1} - (Q^{n+1,m} - Q^n) \end{aligned}$$

Linearization at iteration level $m+1$ gives

$$E_x^{n+1,m+1} = E_x^{n+1,m} + \left(\frac{\partial E_x^{n+1}}{\partial Q}\right)^m \delta Q'$$

where the flux Jacobian has been frozen at iteration m. Substitution yields

$$I\delta Q' = -\Delta\tau E_x^{n+1,m} - \Delta\tau\frac{\partial}{\partial x}A^{n+1,m}\delta Q' - (Q^{n+1,m} - Q^n)$$

Rearranging results in

$$\left[I + \frac{\Delta\tau}{\Delta x}A^{n+1,m}\right]\delta Q' = -(Q^{n+1,m} - Q^n + \Delta\tau E_x^{n+1,m})$$

which reverts to the standard noniterative form when no subiterations are taken, as can be seen by substitution of n for $n+1, m$.

The temporally second-order accurate representation is found by extension of the above procedure. Using a three-point backward time stencil,

$$Q_t = C_0 Q^{n+1} + C_1 Q^n + C_2 Q^{n-1}$$

where

$$\begin{aligned} C_0 &= \frac{1-\sigma}{(1-\sigma)\Delta\tau_2 + \Delta\tau_1}, \quad C_1 = \frac{\sigma}{(1-\sigma)\Delta\tau_2 + \Delta\tau_1} \\ C_2 &= \frac{-1}{(1-\sigma)\Delta\tau_2 + \Delta\tau_1} \end{aligned}$$

and $\sigma = (1 + \Delta\tau_1/\Delta\tau_2)^2$. The elapsed time between the $n-1$ and n time levels is given by $\Delta\tau_1$ and the step size between n and $n+1$ is $\Delta\tau_2$. Finally,

$$\left[I + \frac{1}{C_0\Delta x}A^{n+1,m}\right]\delta Q' = \\ -(Q^{n+1,m} + \frac{C_1}{C_0}Q^n + \frac{C_2}{C_0}Q^{n-1}) - \frac{1}{C_0}E_x^{n+1,m}$$

which again reduces to the special noniterative case. The use of a variable time step allows the solution to progress using a constant Courant number, possibly preventing inadvertent divergences. Higher-order accuracy in time may be determined by extension of the above technique, albeit with additional memory requirements.

The assertion that this technique reduces the factorization and linearization errors is substantiated as follows. The right hand side of the method contains the discretized governing equations in their pure form, that is, without the numerical approximations utilized to attain rapid convergence. The left hand side allows the use of large time steps by relieving the Courant-Friedrichs-Lewy stability constraint. Deferring the question of uniqueness, if a set of dependent variables is found such that the right hand side is satisfied, then this field is a solution to the discretized equations regardless of the approximations made to arrive at that set.

Grid Generation

Grid generation is a significant portion of the effort spent in obtaining the flowfield about any reasonably complex geometry. A structured approach is utilized in this study, with the generalized grids generated using codes written by Steinbrenner, Chawner, and Fouts,[22] and Atwood and Vogel.[23] The cases chosen here were, to a certain extent, driven by the anticipated time costliness of the surface definition and mesh generation.

Boundary Conditions

The block implicit boundary conditions are implemented in a manner consistent with the previously described flux split linearization described earlier. The inviscid and viscous impermeable wall conditions are prescribed similarly to those given by MacCormack.[24] Although the following procedures are presented for a cell face which lies along a constant ξ plane, the procedure may be generalized for application to any cell boundary.

The inviscid, impermeable boundary condition is described for a pair of cells between which the surface lies, depicted in Fig. 3. In the following discussion, the cell above the wall will be denoted by subscript 2, the cell below the wall by subscript 1. At cell centroid 2 the velocity is expressed as

$$\vec{V}_2 = u\mathbf{i} + v\mathbf{j} + w\mathbf{k}|_2$$

and at the inviscid wall the surface normal is

$$\begin{aligned} \widehat{s}_{wall} &= \frac{1}{||\mathbf{s}||}(s_x\mathbf{i} + s_y\mathbf{j} + s_z\mathbf{k})|_{wall} \\ &= (\widehat{s}_x\mathbf{i} + \widehat{s}_y\mathbf{j} + \widehat{s}_z\mathbf{k})|_{wall} \end{aligned}$$

hence the velocity component normal to the wall is

$$\begin{aligned} \vec{V}_{n2} &= ||\vec{V}_{n2}||\widehat{s}_{wall} \\ &= (u\widehat{s}_x + v\widehat{s}_y + w\widehat{s}_z)(\widehat{s}_x\mathbf{i} + \widehat{s}_y\mathbf{j} + \widehat{s}_z\mathbf{k}) \end{aligned}$$

Since, $\vec{V} = \vec{V}_t + \vec{V}_n$, then the tangential velocity component is

$$\begin{aligned} \vec{V}_{t2} &= \vec{V}_2 - \vec{V}_{n2} \\ &= [u - \widehat{s}_x(u\widehat{s}_x + v\widehat{s}_y + w\widehat{s}_z)]\mathbf{i} \\ &\quad + [v - \widehat{s}_y(u\widehat{s}_x + v\widehat{s}_y + w\widehat{s}_z)]\mathbf{j} \\ &\quad + [w - \widehat{s}_z(u\widehat{s}_x + v\widehat{s}_y + w\widehat{s}_z)]\mathbf{k}|_2 \end{aligned}$$

The inviscid condition is satisfied by $\vec{V}_{t1} = \vec{V}_{t2}$, while $\vec{V}_{n1} = \vec{V}_{n2}$ specifies the impermeable condition. Reflecting total energy and density as even functions, then a Riemann problem can be solved at the wall to determine the flux. This amounts to the wall being represented as a contact discontinuity by constraining the contravariant velocity to vanish. Implicitly, this results in

$$\delta Q_1 = R^{-1}ER|_{wall}\delta Q_2 \tag{4}$$

where

$$R^{-1}ER = \begin{bmatrix} 1 & 0 & 0 & 0 & 0 \\ 0 & 1-2\hat{s}_x^2 & -2\hat{s}_x\hat{s}_y & -2\hat{s}_x\hat{s}_z & 0 \\ 0 & -2\hat{s}_y\hat{s}_x & 1-2\hat{s}_y^2 & -2\hat{s}_y\hat{s}_z & 0 \\ 0 & -2\hat{s}_z\hat{s}_x & -2\hat{s}_z\hat{s}_y & 1-2\hat{s}_z^2 & 0 \\ 0 & 0 & 0 & 0 & 1 \end{bmatrix}$$

The block tridiagonal system may be written as

$$\begin{bmatrix} B_1' & C_1' & \\ A_2' & B_2' & C_2' \\ & & \ddots \end{bmatrix} \begin{bmatrix} \delta Q_1 \\ \delta Q_2 \\ \vdots \end{bmatrix} = \begin{bmatrix} \Delta Q_1 \\ \Delta Q_2 \\ \vdots \end{bmatrix}$$

Now the change in flux across an arbitrary cell wall boundary is given by $\Delta E_{wall} = A^+\delta Q_1 + A^-\delta Q_2$, or the sum of the changes in the flux contribution from the positive and negative moving waves. Substitution of Eq. (4) yields

$$\Delta E_{wall} = (A^+R^{-1}ER + A^-)\delta Q_2$$

and it can be seen that dependence upon δQ_1 has been eliminated. Hence, the block tridiagonal system may be represented with embedded boundary conditions as

$$\begin{bmatrix} B'' & C_2' & \\ A_3' & B_3' & C_3' \\ & & \ddots \end{bmatrix} \begin{bmatrix} \delta Q_2 \\ \delta Q_3 \\ \vdots \end{bmatrix} = \begin{bmatrix} \Delta Q_2 \\ \Delta Q_3 \\ \vdots \end{bmatrix}$$

where B'' is the appropriately modified Jacobian.

The viscous impermeable wall imposes additional constraints on the specification of the wall flux. Again utilizing a primitive variable vector $V = [\rho, u, v, w, \epsilon]^T$, then

$$\delta V_1 = diag[1, -t_u, -t_v, -t_w, -t]\delta V_2 = \frac{\partial V_1}{\partial V_2}\delta V_2$$

for a wall face at $\frac{3}{2}$. In this form the toggles t_u, t_v, t_w, and t are set at -1 or 1 for a slip or a no-slip condition, or adiabatic or isothermal wall, respectively. This may be seen by simply rearranging expressions of the form $u_{wall} = \frac{1}{2}(u_1 + u_2)$ or $u_{wall} = u_1 = u_2$. Having already specified the impermeable wall conditions earlier, only the viscous terms at the wall are of present concern. Looking at the terms of the form

$$\Delta Q_2 = \frac{\Delta t}{\mathcal{V}^2}(-MN_1\delta Q_1 + MN_2\delta Q_2 + \cdots)$$

then substitution of the wall relations above leaves a term

$$\begin{aligned} \Delta Q_2 &= \frac{\Delta t}{\mathcal{V}^2}\left[-M\frac{\partial V_1}{\partial V_2}\frac{\partial V_2}{\partial Q_2}\delta Q_2 + M\frac{\partial V_2}{\partial Q_2}\delta Q_2 + \cdots\right] \\ &= \frac{\Delta t}{\mathcal{V}^2}\left[M\left(I - \frac{\partial V_1}{\partial V_2}\right)\frac{\partial V_2}{\partial Q_2}\delta Q_2 + \cdots\right] \end{aligned}$$

which is subsequently embedded into the block structure. The dependent variables within cell 1 are specified according to boundary-layer theory, holding the pressure gradient zero normal to the wall. The remaining variables follow from fluid and thermodynamic relations.

The class of problems investigated here revealed that the use of block implicit boundary conditions resulted in significantly enhanced convergence. This beneficial effect is caused by the faster signal propagation arising from the incorporation of the boundary conditions within the linear system.

Results and Discussion

The methods introduced in the previous sections are applied to test cases which demonstrate the capabilities of the algorithm. The viscous term treatment in a low Mach number regime is shown in the Couette flow problems, which are compared to similarity solutions and previously obtained numerical results. Demonstration of the inviscid term treatment is shown by the capturing of transient discontinuities in the shock tunnel starting problem. The three-dimensional results are compared with an experimental study of a hemicylinder mounted in a shock tube.

The Couette flow problem is used to compare the present method against the method of Beam and Warming[25] and the similarity solution as given by Schlichting.[26] The solutions shown in Fig. 4 were obtained using quiescent initial conditions and viscous boundary conditions with no-slip adiabatic walls. Both of these cases were implemented in the thin-layer form at a Reynolds number of 6.4, based on the distance between the plates, equal to 10^{-5} feet. During the course of these solutions, slightly more than an order of magnitude drop in $||\rho||_\infty$ per two subiterations was observed in the (3×10) cell domain. The Courant number used for the oscillating plate calculation was approximately 10, indicating the viability of these types of unsteady computations at Courant numbers greater than unity. The Courant number was computed using $\nu = \frac{\Delta t}{\mathcal{V}} max[|(\widehat{U}, \widehat{V}, \widehat{W})| + c]||s||$ over each cell in the domain. Identical results were obtained using both the two- and three-dimensional implementations in all directional permutations. Results reveal steeper gradients than that of the conventionally differenced scheme or the analytic solution, a possible consequence of the handling of the boundary conditions or the viscous term treatment. In addition, this case was found to be insensitive to the choice of the higher-order flux correction terms, possibly because of the dominance of diffusive effects.

The third test case evaluated the inviscid term treatment through the simulation of the transient starting process of a planar shock tunnel. The (300 × 60) cell domain is shown in Fig. 5. The solution of the Euler equations is presented in Fig. 6 as a comparison of the experimental and numerical shadowgraph images, the former due to Amann,[27] while the graphical presentation of the latter is due to Buning.[28] This solution was obtained using Roe flux difference splitting with $\phi = 1/3$, the upwind biased flux evaluation. The Steger-Warming flux evaluation with Roe averaging was found to be moderately less stable, but no significant differences in the results were found for this case. The maximum compression parameter was used, and the entropy-fix parameter used in Harten's formulation was set to 0.15. Disconcertingly nonphysical solutions were produced for smaller entropy-fix levels, possibly associated with an entropy-violating condition. The problem was initialized with a moving shock propagating to the right at a Mach number of 2.97, while the boundary conditions were specified as impermeable inviscid along the walls and fixed for the inlet and exit. For the maximum Courant number of four used here, four subiterations were chosen per time step based on a subjective judgment of discontinuity sharpness. The $||\rho||_\infty$ was observed to drop approximately an order of magnitude over the course of these four subiterations.

Physically, this nozzle starting process generates a reservoir of more than 50 times the initial pressure, while the density increases by 11 times the initial state. This reservoir provides the energy necessary to generate high Mach flows in the diverging nozzle region for short durations. The ensuing reflections of the shock with the nozzle wall reveals the complexities of the shock-shock and shock-contact interaction. In particular, it can be seen that the development of the rearward-facing shock, which is directed upstream while being swept downstream, is resolved. At later times, the finer scale fluid motion between the primary and rearward facing shocks is for the most part lost because of grid coarseness and attendant numerical dissipation. However, increasingly fine structures are captured as the grid is refined.

The viability of the technique in three dimensions is shown by the final test cases. These results are intended to replicate the conditions in an experimental study of a hemicylinder in a shock tube by Kingery and Bulmash.[29] The experiment test configuration and pressure transducer locations are shown in Figs. 7 and 8. In order to estimate the costs and benefits of inviscid versus viscous simulations, the flow about this geometry was computed using both the Euler and Navier-Stokes equations. However, the expense of these three-dimensional simulations permitted the use of only one of the inviscid flux evaluation methods; the Roe flux difference splitting was chosen.

The simulation was initialized as a planar shock translating at a Mach number of 1.518 before diffraction over the cylinder began. The Reynolds number per meter was 23.3×10^6, computed using $T_\infty = 288.17\,K, p_\infty = 101\,325\,N/m^2$, and specifying the reference velocity based on the quiescent state. Boundary conditions are specified for the viscous, single zone computation as follows. In the ξ-direction, extrapolation is used. This nonphysical extrapolation is adequate for the duration of the early interaction. However, solutions at larger times are suspect, where times after the shocks have propagated through the boundaries are defined as large. Additionally, the use of an advancing front boundary is enabled because of a priori knowledge of the grid structure and the primary shock speed. This simple time-dependent boundary reduces the computational time requirements. In the η-direction, the lower boundary defines the surface geometry of the hemicylinder, and hence is specified as a no-slip isothermal wall. The top of the domain in the η-direction, corresponding to the inner radius of the shock tube, is specified as an inviscid wall, based on the assumption that the viscous effects on this surface have negligible influence on the results. Finally, the ζ-direction boundaries are treated using the viscous condition along the floor of the tube. Symmetry conditions are used along the plane running along the longitudinal axis of the cylinder and normal to the floor. To simulate experimental conditions, the wall temperature was set equal to the temperature of the quiescent flow prior to primary shock arrival. The viscous grid has normal spacing of approximately 10^{-5} meters at the viscous walls. The Euler computation used the inviscid boundary conditions previously discussed where appropriate. For this Euler grid, since the areas of the faces corresponding to the geometric axis singularity are zero then $\vec{F} \cdot \mathbf{s}$ is also zero. Compensation for the round-off error inherent in the grid was implemented by eliminating those face areas which fell below a specified tolerance. The grids and boundary conditions for these cases are partly shown in Figs. 9 and 10.

The inviscid computation used $\phi = 1/3$, $\beta = 4$, Harten's entropy fix parameter of 10^{-4}, Roe flux difference splitting, one subiteration per second-order accurate time step, and a Courant number of 15. The solution was obtained in 1500 time steps without any change of parameters.

The viscous computation used the same flux evaluation as above with the addition of the second-order accurate full viscous terms. Because of the viscous spacing, the Courant number utilized was 10^4, allowing the solution to be obtained in 6800 time steps with no subiterations. In contrast to the inviscid simulation, the advancing front boundary condition was utilized in this case.

Results, given in Figs. 11 through 16, show that the primary shock is captured over two to three cells, the large physical thickness obtained is an artifact of the coarse grid used. Adaptive gridding methods would help maintain sharp shocks, but the anticipated expense of these methods precluded their use here. Figures 11 and 12 show comparisons of the numerical and experimental pressure histories. It is seen that the peak overpressure is underpredicted by 10%, possibly owing to the coarseness of the grid which in turn thickens the shock. This thickening causes the potential energy in the form of pressure to be transferred to the surface over several time increments. These computed surface pressures were extracted from the domain through the use of a Newton search in three-space for the cell in which the given (x, y, z) probe coordinate fell.[28] Subsequent trilinear interpolation over the cell, where the uniform parametric coordinates (u, v, w) are determined from the positions of the vertices of the hexahedral cell, allows the pressure to be computed. Inherent in this first-order approximation lies the assumption that over a discrete cell the variation of pressure is linear in space.

Figures 13 through 16 show portions of the viscous simulation at selected times. Physically, the interaction process begins with the normal impact of the incident shock with the front face of the hemicylinder. At this time, peak overpressures of six times, and densities of four times that of the quiescent state are generated along this forward face. As the shock diffracts over the sharp corner of the target, a separation bubble forms, which eventually envelops a large portion of the circumferential face of the body. This vortical motion is depicted in Fig. 16 by instantaneous streamlines. A supersonic pocket is generated as the air negotiates the sharp corner as it rushes from the stagnation region left in the wake of the upstream propagating reflected shock. The next significant event occurs as the shock diffracts over the rearward face, shedding a strong vortex sheet while an expansion wave propagates away in a pattern which grows with time. The diffracted shock then impacts the floor of the shock tube, reflecting it upwards, while the shock which diffracted over the circumferential face reflects inwards from the outer walls of the tube. The subsequent diffractions and reflections result in the interaction of shocks, expansion fans, vortices, and developing boundary layers. From experimental evidence, this gross unsteadiness does not dissipate for more than 15 milliseconds after the interaction event begins. However, the primary shock passes from the test section 5 milliseconds after the initial target interaction; therefore, the computation is stopped at that time.

The effects of the viscous terms are seen by comparing the pressure histories in Figs. 11 and 12. While the pressures along the upstream face are largely unchanged, the circumferential and downstream faces are significantly affected by viscosity. The large separation along these faces causes low pressure regions due to this vortical motion. This phenomenon is more accurately captured in the viscous simulation, as may be seen by inspection of the pressure histories at probe 11. Differences between the experimental and the present results may be due to poor capturing of the vortex strength owing to grid coarseness. However, the higher-order behaviour of the method used here attempts to reduce the need for finely spaced meshes. In addition, the occurrence of deformation of the shroud wall is thought to be a possible event during the experiment.[30]

A limited cost/benefit study of the Euler versus Navier-Stokes equations was also performed for the hemicylinder case. For approximately 5.5 ms of flow history on a $(78 \times 50 \times 25)$ cell grid, the Euler computation consumed 7.6 processor hours, while the viscous simulation required 18.2 hours. From these results, the somewhat more accurate solution given by the Navier-Stokes simulation may be worthwhile. This is particularly true if the flowfield behaviour after primary shock passage is important.

Conclusions

The application of two upwind schemes to unsteady, multidimensional problems within a structured finite-volume framework has been demonstrated on the viscous three-dimensional blast-wave problem. The use of time-conservative differencing and an approximate Riemann solver coupled with total variation diminishing methods has resulted in time accurate nonoscillatory flowfield resolution. Newton subiterations are utilized to reduce the numerical approximations made, such as factorization error and the inclusion of only the first-order terms in the formation of the inviscid Jacobian. In addition, analysis and application of two flux evaluation methods found their differences to be small. Finally, for the blast-wave/target interaction problem the effect of viscosity was increasingly significant at later times.

The expense of these algorithms is relatively high: $86\mu s$ per cell per iteration using a single processor on the Ames Research Center CCF Cray Y-MP/832 for these vectorized codes which have computation rates of approximately 142 MFLOPS. In addition, the memory requirement is 38 words per cell. Decreased processor times may be achieved by many schema. Freezing the Jacobian for several subiterations will offer a processing time reduction of 15% per subiteration, albeit at the expense of memory.

While the additional computational cost of these algorithms may be justified only for cases requiring their capabilities, the expenditure of human effort is likely to be less than with conventionally differenced techniques because of the natural scaling of the dissipation with the eigensystem. This feature provides somewhat greater freedom from the numerics, permitting the scientist to concentrate on the physical problem and the engineer on design.

Further efforts to increase the accuracy and efficiency of these methods may be directed along the use of nonfactored schemes or implementation on parallel machines. Geometries of realistic complexity will require a zonal approach, necessarily conservative because of the strongly unsteady compressible flow regimes considered here. Efficient adaptive grid techniques will reduce the memory and time expense. Synthesis of dynamical, structural, and fluid flow effects may provide the capability for an interdisciplinary simulation of the physical processes involved in this class of problems.

The development of this type of tool partially fulfills the objective of augmentation of experimental test programs, possibly eliminating the need to test certain specific configurations altogether. Although the use of the inviscid flowfield time history is feasible in the design process, the goal of nesting full unsteady Navier-Stokes methods within this cycle awaits the advent of computers of increased power.

Acknowledgements

Support for this investigation was provided by the Army Ballistic Research Laboratory under contract NCC 2-540.

References

[1] Champney, J.M., Chaussee, D.S., and Kutler, P., "Computation of Blast Wave - Obstacle Interactions," AIAA-82-0227, January 1982.

[2] Mark, A., and Kutler, P., "Computation of Shock Wave/Target Interaction," AIAA-83-0039, January 1983.

[3] Löhner, R., "The Efficient Simulation of Strongly Unsteady Flows by the Finite Element Method," AIAA-87-0555, January 1987.

[4] Yee, H.C., "Upwind and Symmetric Shock-Capturing Schemes," NASA TM-89464, May 1987.

[5] Bennett, B.C., Abbett, M.J., and Wolf, C.J., "Viscous Effects of Blast Wave Flowfields," AIAA-86-0031, January 1986.

[6] Molvik, G.A., "Computation of Viscous Blast Wave Solutions with an Upwind Finite Volume Method," AIAA-87-1290, June 1987.

[7] Hisley, D., and Molvik, G.A., "Axisymmetric Calculations for the Large Blast/Thermal Simulator (LB/TS) Shock Tube Configuration," BRL-TR-2935, September 1988.

[8] Vinokur, M., "An Analysis of Finite-Difference and Finite-Volume Formulations of Conservation Laws," NASA CR-177416, June 1986.

[9] Steger, J.L., "Implicit Finite-Difference Simulation of Flow about Arbitrary Two-Dimensional Geometries," *AIAA J.*, Vol. 16, July 1978, pp. 679-686.

[10] Warming, R.F., Beam, R.M., and Hyett, B.J., "Diagonalization and Symmetrization of the Gas-Dynamic Equations," *Math. Comp.*, Vol. 29, October 1975, pp. 1037-1045.

[11] Steger, J.L., and Warming, R.F., "Flux Vector Splitting of the Inviscid Gasdynamic Equations with Application to Finite-Difference Methods," *J. Comp. Phys.*, Vol. 40, 1981, pp. 263-293.

[12] Barth, T.J., "Analysis of Implicit Local Linearization Techniques for Upwind and TVD Algorithms," AIAA-87-0595, January 1987.

[13] Godunov, S.K., "Difference Method of Numerical Computation of Discontinuous Solutions of Hydrodynamic Equations," *Mat. Sb.*, Vol. 47, 1959. pp. 271-306.

[14] Roe, P.L., "Approximate Riemann Solvers, Parameter Vectors, and Difference Schemes," *J. Comp. Phys.*, Vol. 43, 1981. pp. 357-372.

[15] MacCormack, R.W., "Lecture Notes on the Numerical Computation of Compressible Viscous Flow," Stanford Univ., January 1986.

[16] Chakravarthy S.R., and Osher, S., "High Resolution Applications of the Osher Upwind Scheme for the Euler Equations," AIAA-83-1943.

[17] Chakravarthy, S.R., "A New Class of High Accuracy TVD schemes for Hyperbolic Conservation Laws," AIAA-85-0363, January 1985.

[18] Yanenko, N.N., *The Method of Fractional Steps: The Solution of Problems of Mathematical Physics in Several Variables*, (M. Holt, ed.), Springer-Verlag, New York, 1971.

[19] Chakravarthy, S.R., "Relaxation Methods for Unfactored Implicit Upwind Schemes," AIAA-84-0165, January 1984.

[20] Rai, M.M., and Chakravarthy, S.R., "An Implicit Form for the Osher Upwind Scheme," *AIAA J.*, Vol. 24, May 1986. pp. 735-743.

[21] Rogers, S.E., and Kwak, D., "An Upwind Differencing Scheme for the Time-Accurate Incompressible Navier-Stokes Equations," AIAA-88-2583, June 1988.

[22] Steinbrenner, J.P., Chawner, J.R., and Fouts, C.L., "A Structured Approach to Interactive Multiple Block Grid Generation," AGARD FDP Specialists Mtg. on Mesh Generation for Complex Three-Dimensional Configurations, Loen, Norway, May 1989.

[23] Atwood, C.A., and Vogel, J.M., "Surface Grid Generation for Flowfield Applications Using B-Spline Surfaces," AIAA-89-2177, August 1989.

[24] MacCormack, R.W., "Current Status of Numerical Solutions of the Navier-Stokes Equations," AIAA-85-0032, January 1985.

[25] Beam, R.H.,and Warming, R.F., "An Implicit Factored Scheme for the Compressible Navier-Stokes Equations," *AIAA J.*, Vol. 16, April 1978, pp. 393-402.

[26] Schlichting, H., *Boundary Layer Theory*, McGraw-Hill, New York, 1979.

[27] Amann, H.O., "Vorgänge beim Start einer ebenen Reflexionsdüse," *Z. Flugwiss*, Vol. 19, 1971, pp. 393-406.

[28] Buning, P.G., and Steger, J.L.,"Graphics and Flow Visualization in Computational Fluid Dynamics," AIAA-85-1507-CP, July 1985.

[29] Kingery, C.N., and Bulmash,G., "Effects of Shock Tube Blockage on Target Loading," BRL-TR-2689, November 1985.

[30] Bulmash,G., Private communication.

57

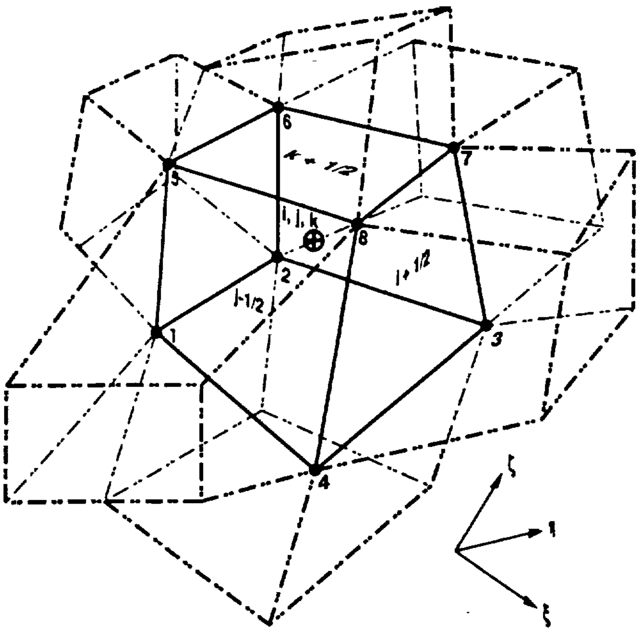

Fig. 1 Discrete hexahedral cell and stencil.

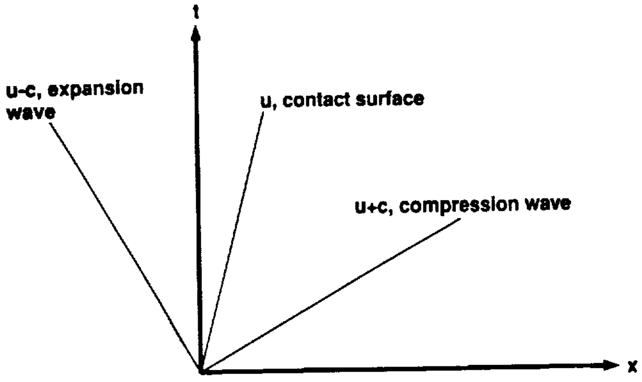

Fig. 2 Schematic of the Riemann problem.

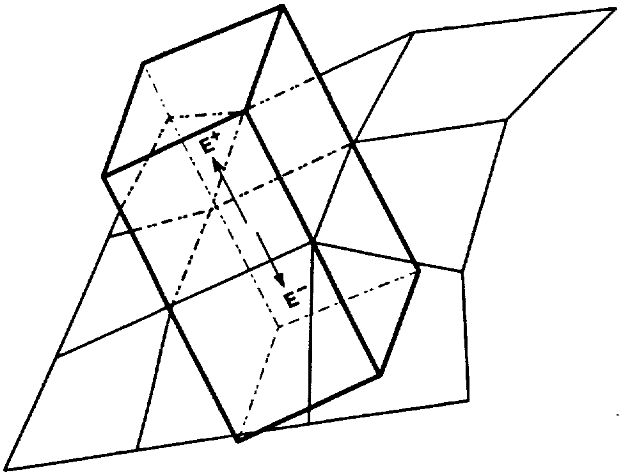

Fig. 3 Flux computation at a cell face or wall.

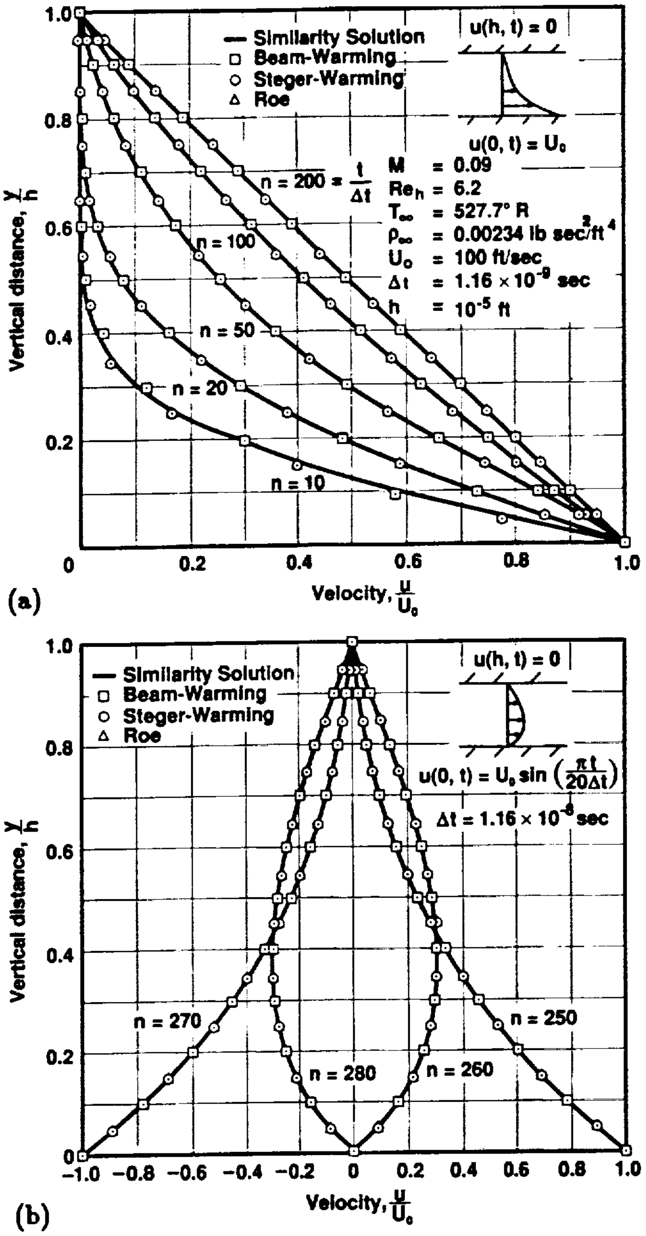

Fig. 4 Couette flow case: (a)Impulsively started and (b)oscillating plate problems.

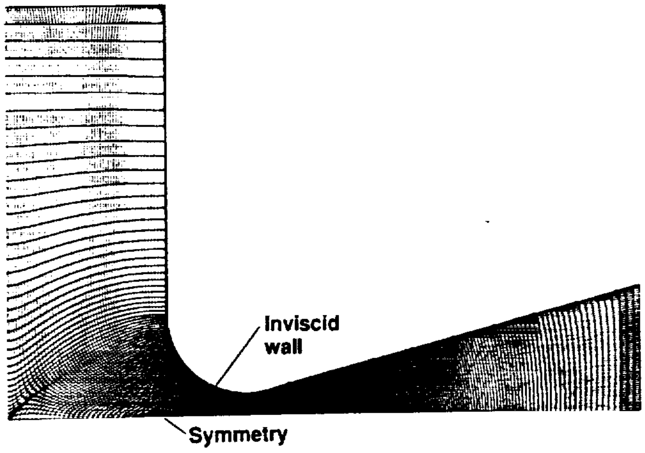

Fig. 5 Shock tunnel case: 300 × 60 cell grid.

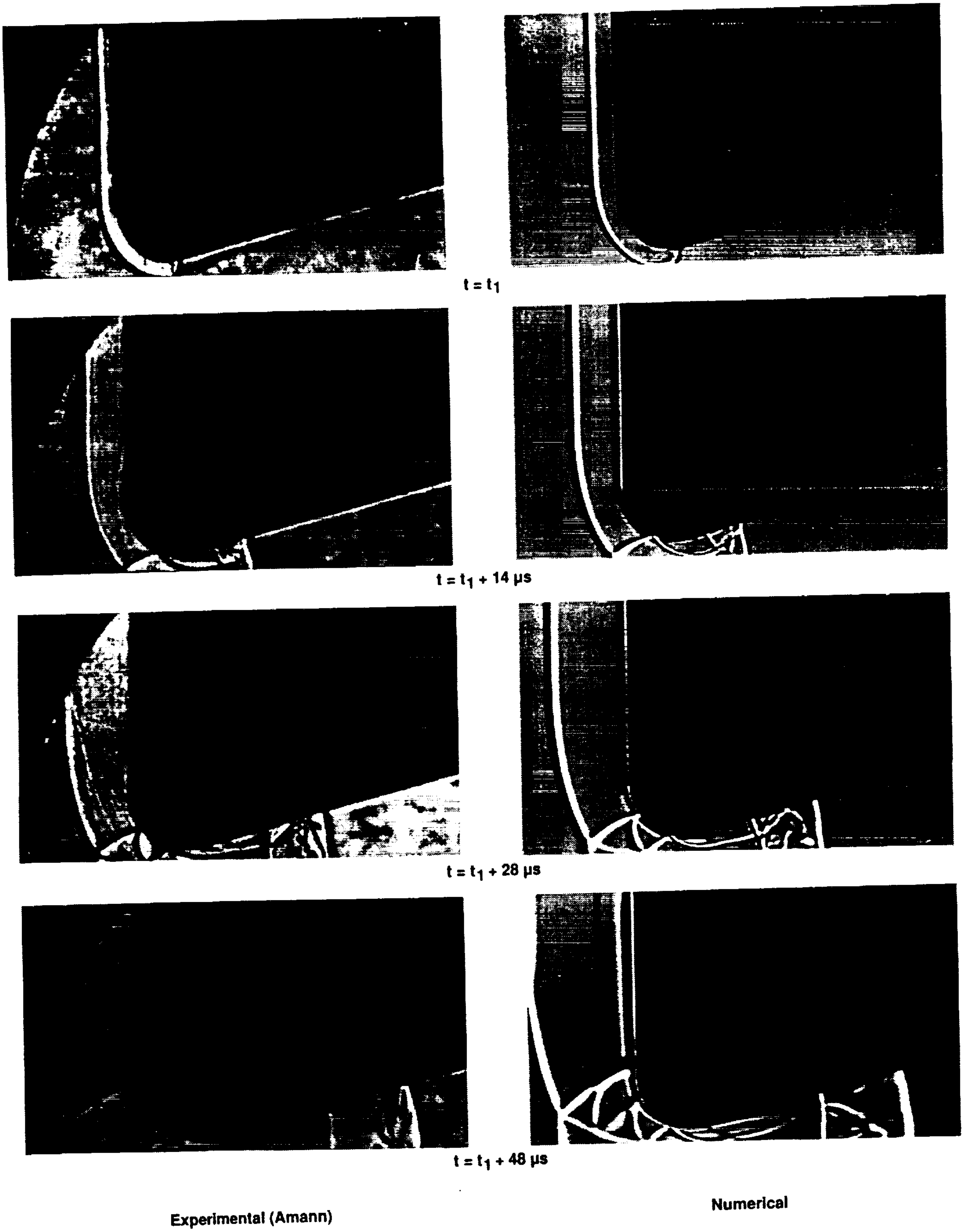

Fig. 6 Shock tunnel case: Shadowgraph comparison for a planar shock with initial speed of Mach 3.

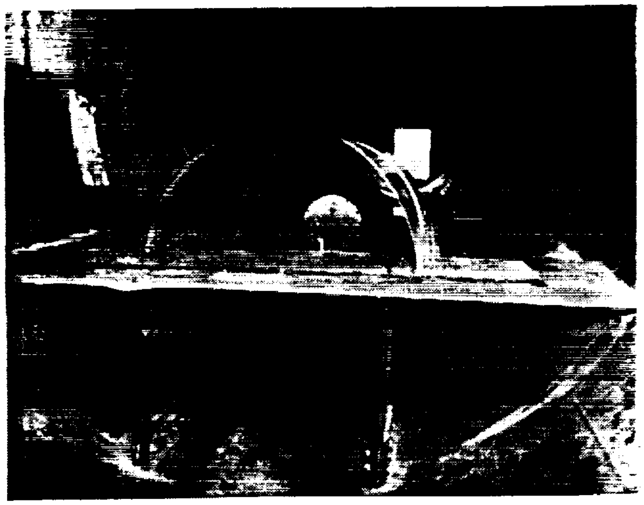

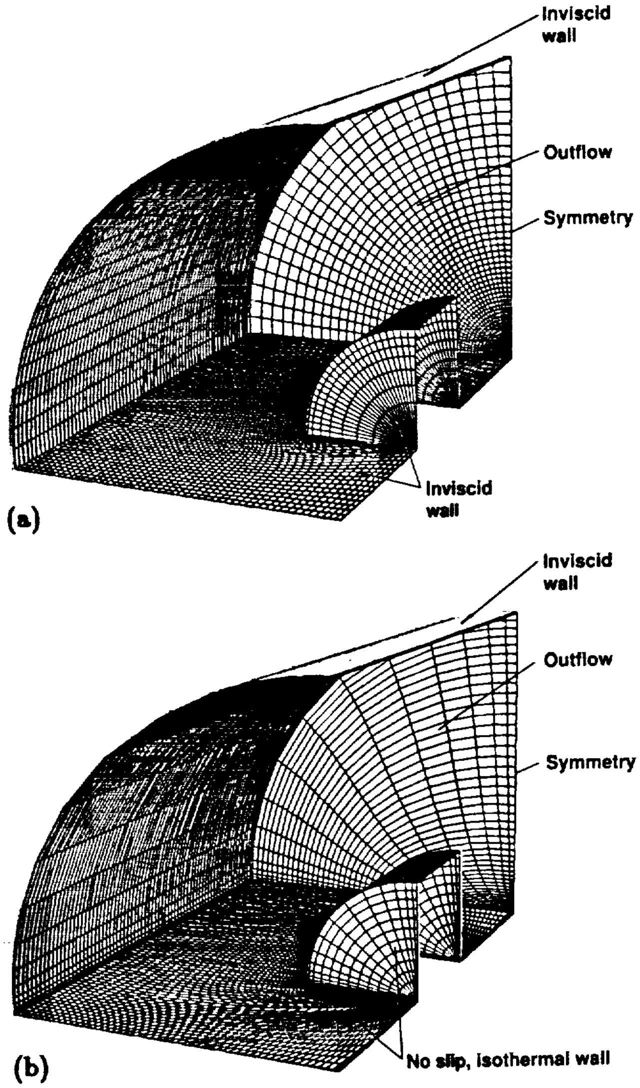

Fig. 9 Hemicylinder case: Central region of the 78 × 50 × 25 cell (a)inviscid and (b)viscid grids.

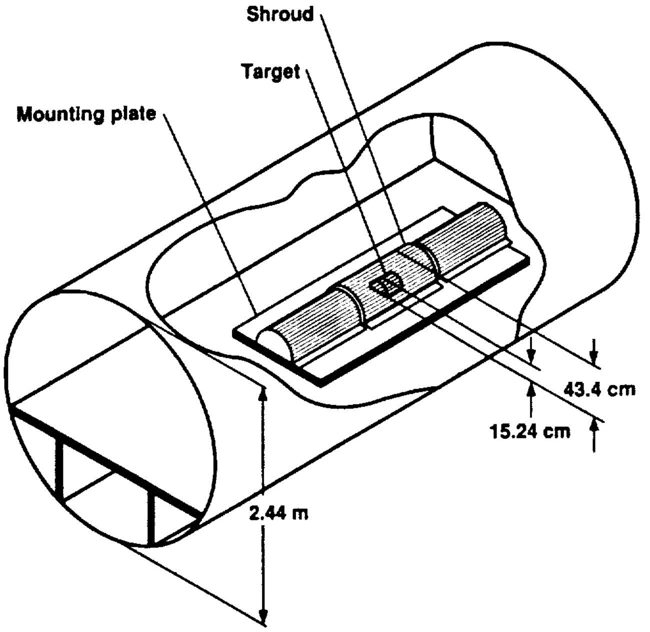

Fig. 7 Hemicylinder case: Experiment configuration (after Kingery and Bulmash).

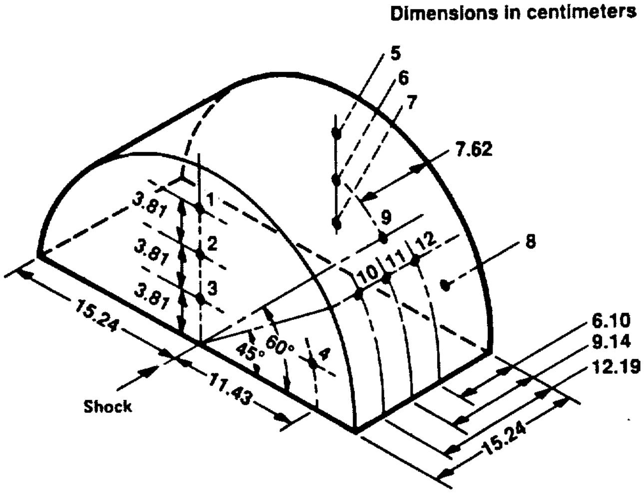

Fig. 8 Hemicylinder case: Pressure transducer locations.

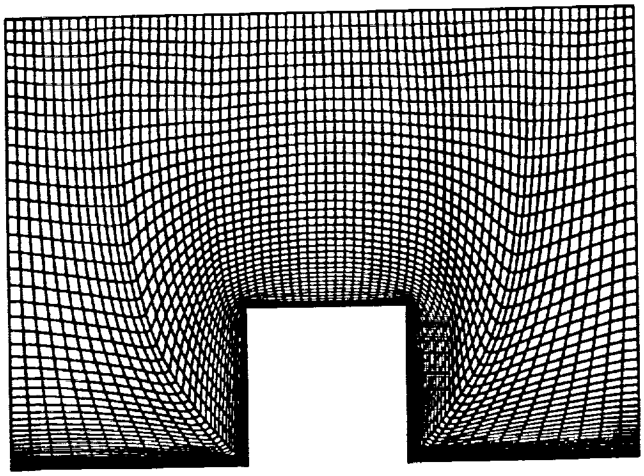

Fig. 10 Hemicylinder case: Symmetry plane of the viscid grid.

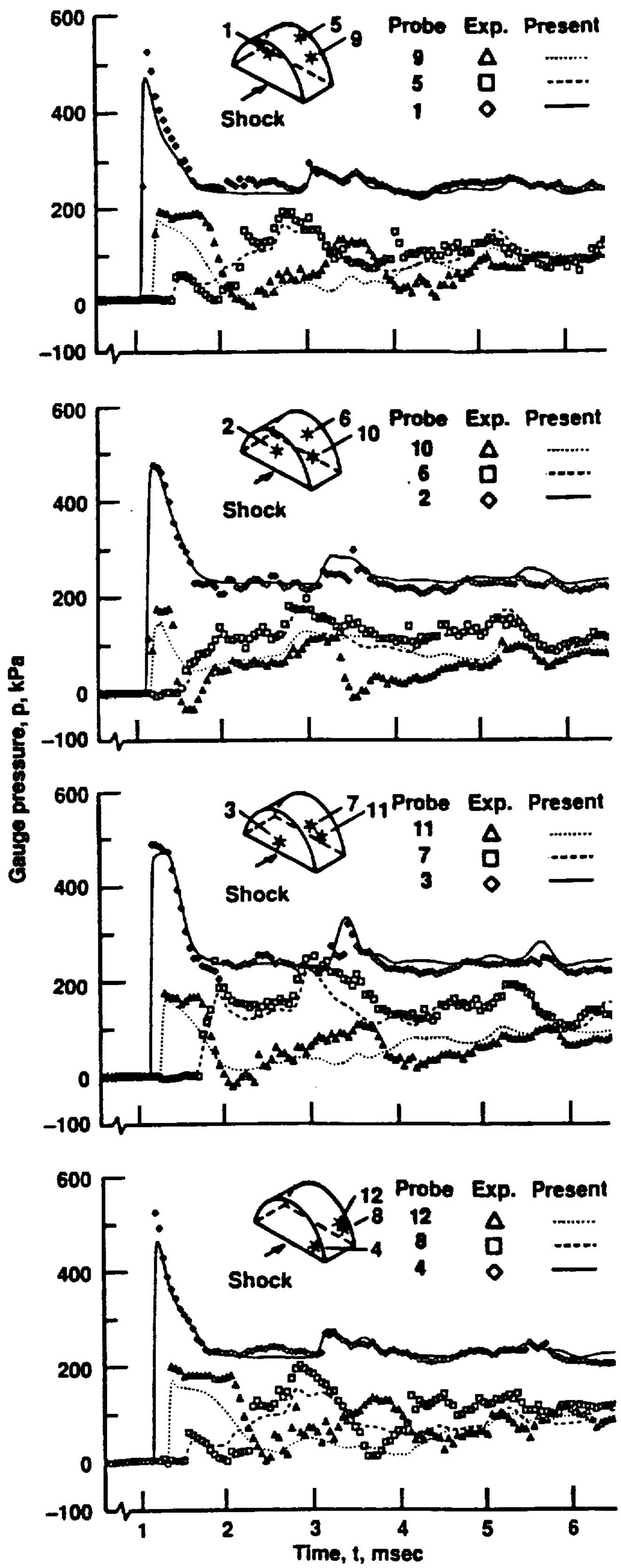

Fig. 11 Hemicylinder case: Experimental and inviscid computation pressure histories.

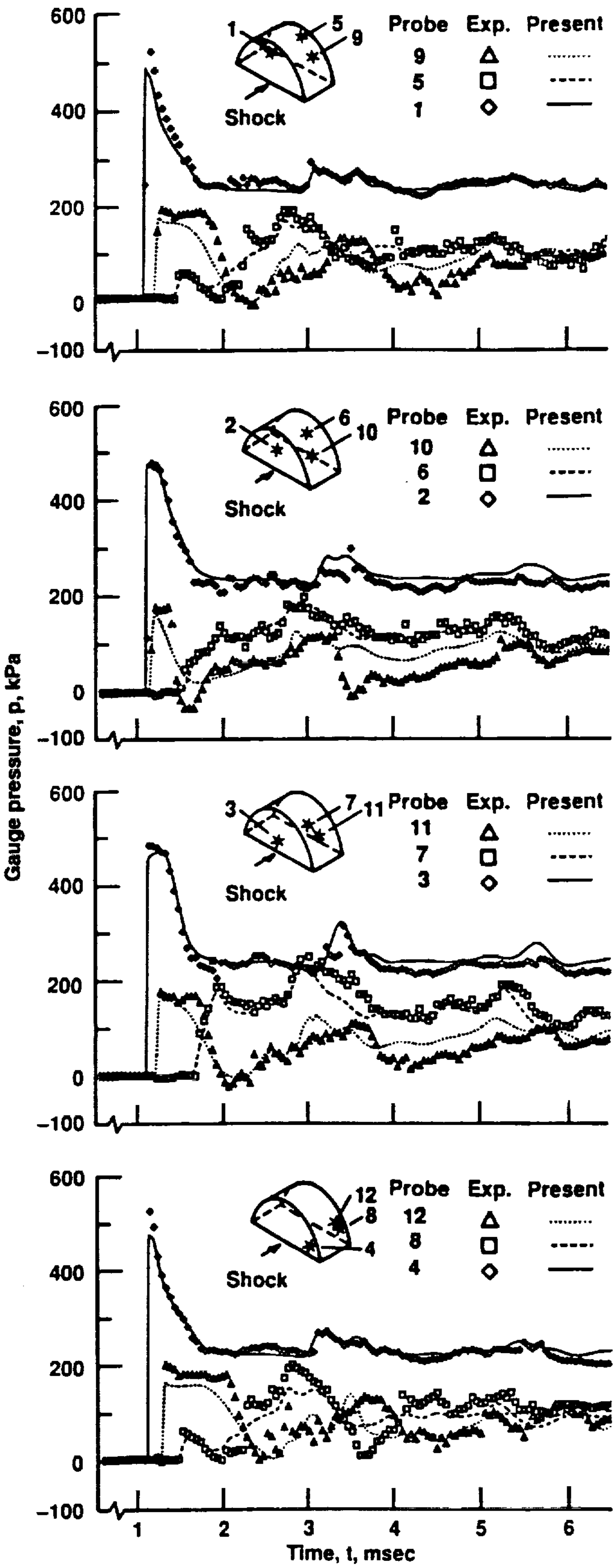

Fig. 12 Hemicylinder case: Experimental and viscous computation pressure histories.

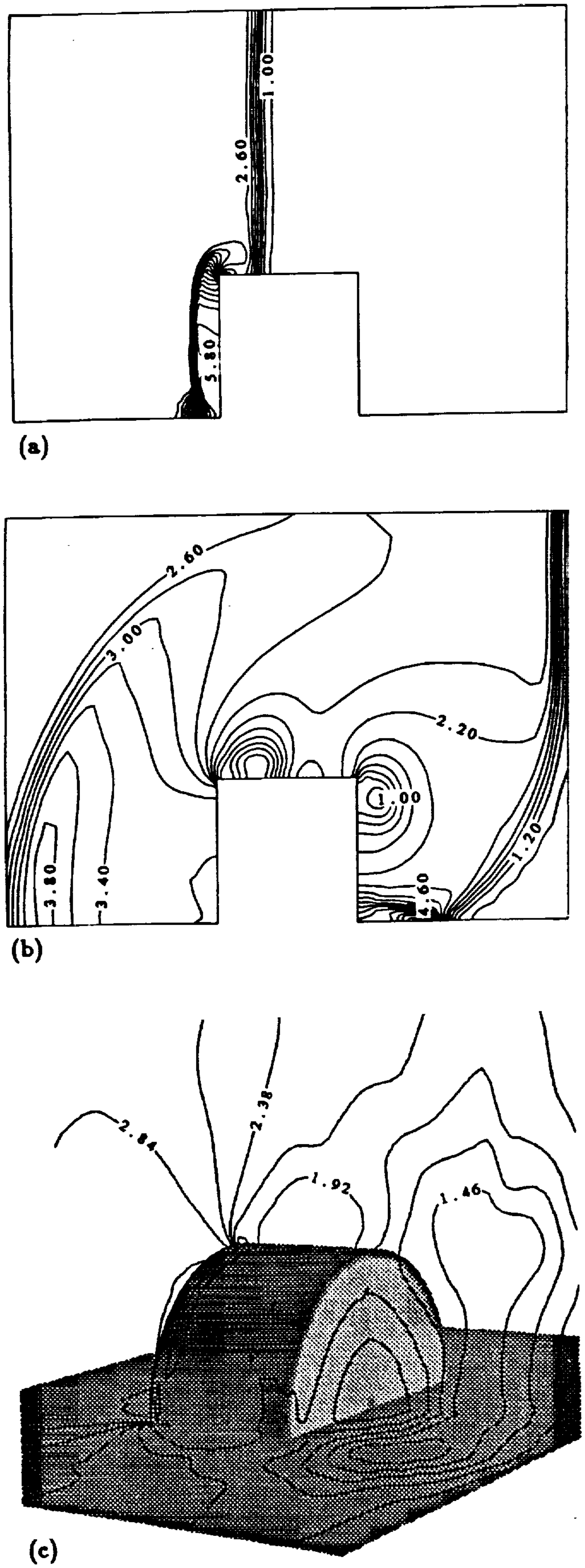

Fig. 13 Hemicylinder case: Pressure contours at (a)t=1.1ms, (b)t=1.7ms, and (c)t=6.2ms.

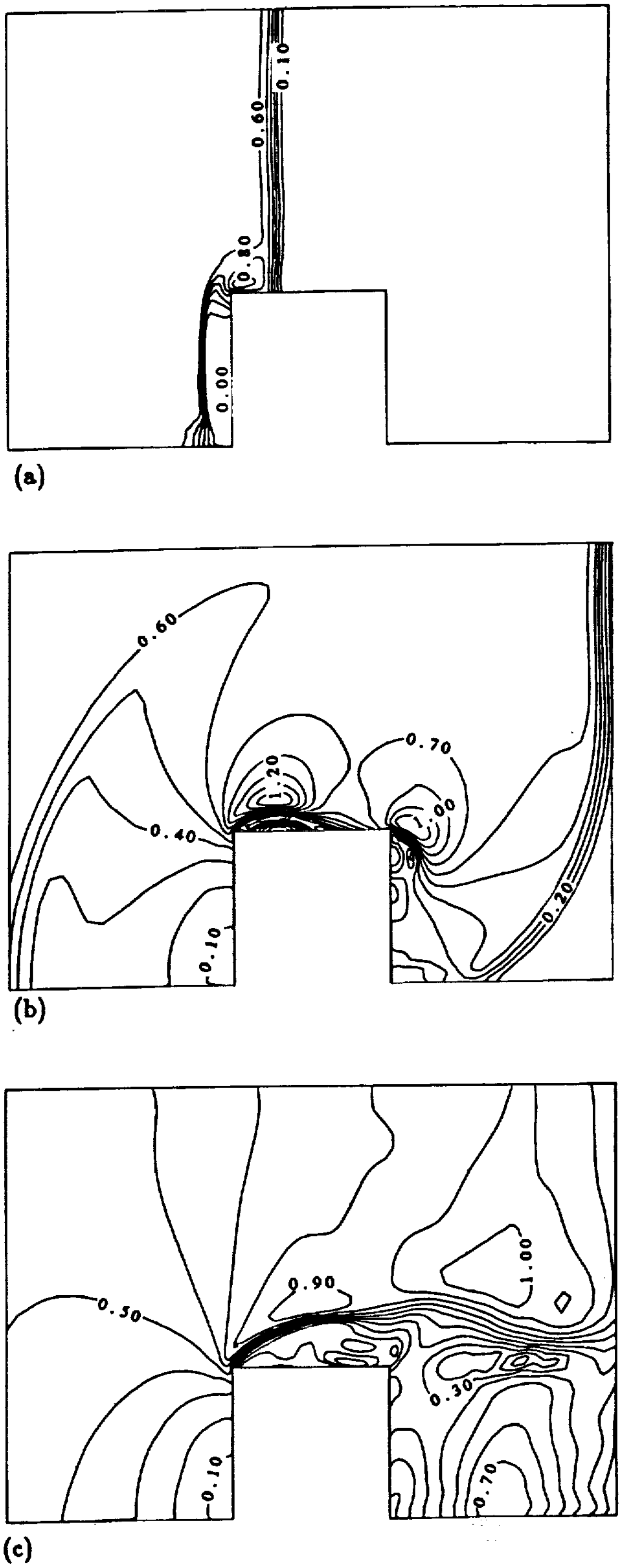

Fig. 14 Hemicylinder case: Symmetry plane Mach contours at (a)t=1.1ms, (b)t=1.7ms, and (c)t=6.2ms.

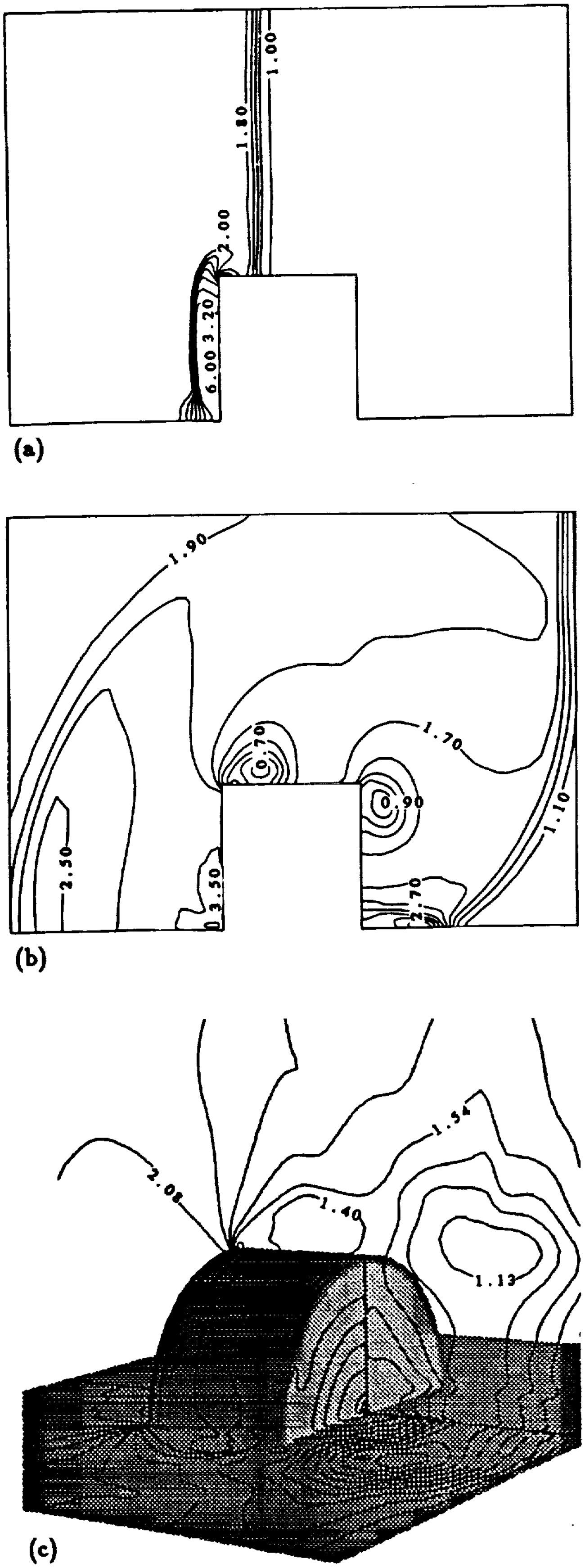

Fig. 15 Hemicylinder case: Density contours at (a)t=1.1ms, (b)t=1.7ms, and (c)t=6.2ms.

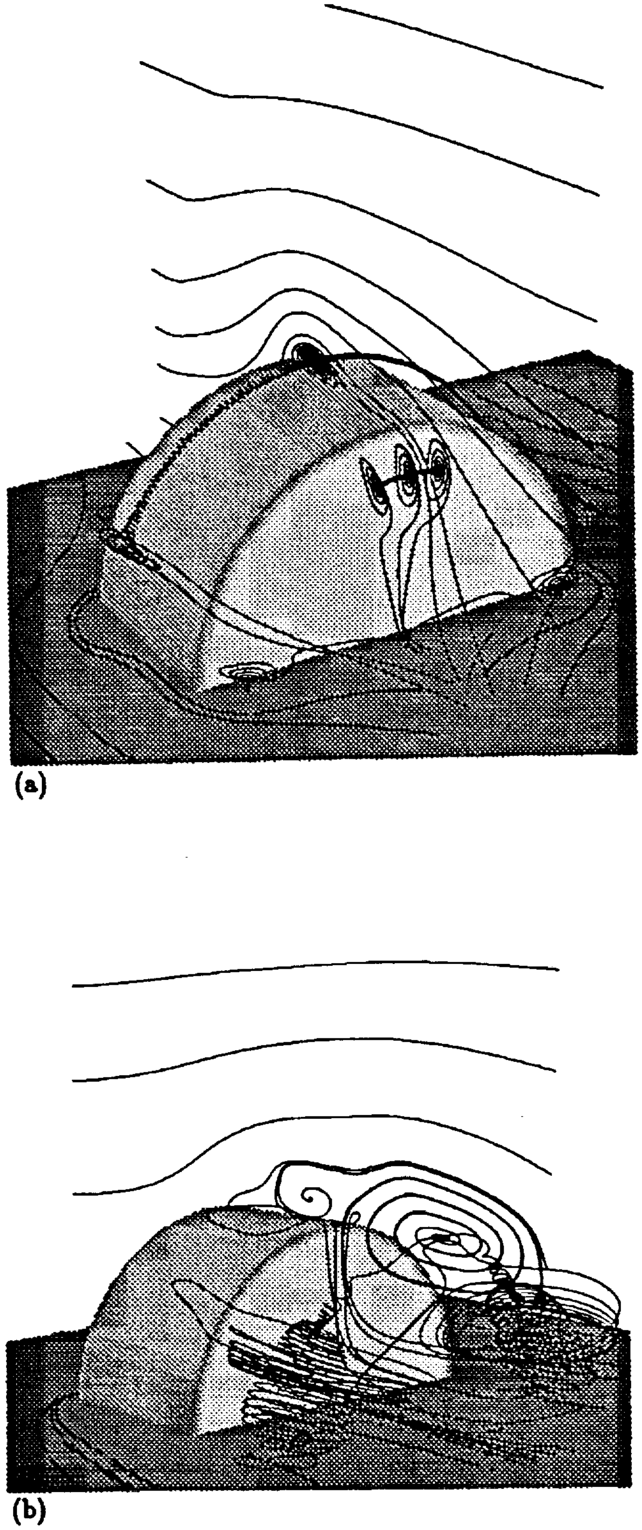

Fig. 16 Hemicylinder case: Instantaneous streamlines at (a)t=1.7ms, and (b)t=6.2ms.

CHRISTOPHER A. ATWOOD

Office address:
M.S. T045-2, NASA Ames Research Center
Moffett Field, California 94035
(415) 604-3974
atwood@fred.nas.nasa.gov

Residence address:
996 Amarillo Avenue
Palo Alto, California 94303
(415) 857-0868

Career Objective

Development and synthesis of computational methods for application to physical problems within an automated design framework.

Educational Background

Stanford University, Ph.D. candidate, Dept. of Aeronautics and Astronautics. 1988-Present.
Iowa State University, Master of Science - Aerospace engineering, May 1988.
Iowa State University, Bachelor of Science - Aerospace engineering, May 1986.

Work Experience

May 1990 - Present: Research Scientist for MCAT Institute at NASA Ames Research Center. Investigator within the Stratospheric Observatory For Infrared Astronomy (SOFIA) project. Application and development of fluid and optical simulation codes.

May 1988 - May 1990: Research Scientist for MCAT Institute at NASA Ames Research Center. Principal investigator of viscous blast wave problem supported on contract from the Army Ballistics Research Laboratory. Development, application and validation of a family of unsteady Navier-Stokes codes in one, two, and three spatial dimensions.

Jan. 1987 - May 1988: Research Assistant at NASA Ames Research Center and at Iowa State University. Development of a preprocessor code to provide high continuity surface definition and mesh generation.

Aug. 1986 - Jan. 1987: Teaching Assistant for Iowa State University. Responsible for instruction and evaluation of junior-level students in an experimental aerodynamics laboratory.

May 1986 - Aug. 1986: Associate Scientist at Douglas Aircraft Corporation, Long Beach, California. Modified and drafted structural components of the C-17 transport aircraft utilizing computer aided design and drafting techniques.

Publications

Atwood, C.A.,"On the Simulation of Unsteady Compressible Flows," NASA CFD Conference, March 1991.

Atwood, C.A.,"An Upwind Approach to Unsteady Flowfield Simulation," AIAA 8th Applied Aerodynamics Conference, August 1990. AIAA-90-3100.

Atwood, C.A., and Vogel, J.M.,"Surface Grid Generation for Flowfield Applications Using B-Spline Surfaces," AIAA 7th Applied Aerodynamics Conference, August 1989. AIAA-89-2177.

Atwood, C.A.,"Geometric Modeling for Flowfield Applications Using Interpolating B-Spline Surfaces, " M.S. Thesis, Department of Aerospace Engineering, Iowa State University, 1988.

References

William R. Van Dalsem, Group Leader, Applied Computational Fluids Branch,
NASA Ames Research Center, Moffett Field, California 94035. (415) 604-4469

Robert W. MacCormack, Professor, Department of Aeronautics and Astronautics,
Stanford University, Stanford, California 94305. (415) 723-4627

Terry L. Holst, Chief, Applied Computational Fluids Branch,
NASA Ames Research Center, Moffett Field, California 94035. (415) 604-6032

Jerald M. Vogel, Associate Professor, Department of Aerospace Engineering,
Iowa State University, Ames, Iowa 50011. (515) 294-6956

William Smith, Section Manager, C-17 Wing Tank Structure,
Douglas Aircraft Corporation, Long Beach, California 90847. (213) 593-1562